1   **Brain-wide mapping of neural activity mediating collicular-dependent behaviors**

2

3   *Arnau Sans-Dublanc[1,2]*, Anna Chrzanowska[1,2]*, Katja Reinhard[1,2,3], Dani Lemmon[1,6], Gabriel Montaldo[1,4],*
4   *Alan Urban[1,2,3,5] and Karl Farrow[1,2,3,4#]*

5   1. Neuro-Electronics Research Flanders. Leuven, Belgium.
6   2. Department of Biology, KU Leuven. Leuven, Belgium.
7   3. VIB. Leuven, Belgium.
8   4. Imec, Leuven, Belgium.
9   5. Department of Neurosciences, KU Leuven. Leuven, Belgium.
10 6. Faculty of Pharmaceutical, Biomedical and Veterinary Sciences, University of Antwerp. Antwerp,
11   Belgium.

12 * These authors contributed equally to this work

13 \# Corresponds should be addressed to karl.farrow@nerf.be

14

Abstract

Neuronal cell-types are arranged in brain-wide circuits to guide behavior. In mice, the superior colliculus is comprised of a set of cell-types that each innervate distinct downstream targets. Here we reveal the brain-wide networks downstream of four collicular cell-types by combining functional ultrasound imaging (fUSi) with optogenetics to monitor neural activity at a resolution of ~100 μm. Each neuronal group triggered different behaviors, and activated distinct, partially overlapping sets of brain nuclei. This included regions not previously thought to mediate defensive behaviors, e.g. the posterior paralaminar nuclei of the thalamus (PPnT), that we show to play a role in suppressing habituation. Electrophysiological recordings support the fUSi findings and show that neurons in the downstream nuclei preferentially respond to innately threatening visual stimuli. This work provides insight into the functional organization of the networks governing defensive behaviors and demonstrates an experimental approach to explore the whole-brain neuronal activity downstream of targeted cell-types.

Introduction

28
29 Different behavioral tasks rely on distinct networks of neurons distributed across the brain.
30 Insights into how specific cell-types are linked to sensation and behavior have seen some great
31 advances through the application of molecular technologies, providing a list of critical circuit
32 elements [1]. On the other hand, computational understanding have been gained by comparing
33 large-scale measurements of brain-wide activity with sensory inputs and behavior [2–5]. However,
34 in mammals the link between individual cell-types, large scale neuronal activity and behavior
35 remains unclear. In the superior colliculus (SC), there is evidence for a strong relationship
36 between individual cell-types and behavior [6–10]. Here, we use this relationship to delineate the
37 cell-type specific brain-wide functional networks that lie downstream of the SC.

38 In mice, the SC is a major hub of visual processing, where the superficial layers of the SC
39 receive direct sensory inputs from >85% of the retinal output neurons [11]. The retino-recipient
40 neurons in the SC contain at least six sets of genetically identified cell-types with distinct
41 anatomy and visual response properties [12–16]. Different cell-types project to different sets of
42 targets, including nuclei of the thalamus and midbrain, thereby forming a putative structural
43 basis for the relationship between cell-types and distinct behavioral properties [6,7,9,12,13,17,18].

44 Optogenetic activation of cell-types in the retino-recipient layers of the colliculus has provided
45 insight into the relationship between output circuits of the SC and behavior. For instance,
46 activation of neurons that project to the pulvinar (LP) has been shown to induce arrest behavior
47 in mice [7,17], while activation of neurons projecting to the parabigeminal nucleus (PBG) leads to
48 flight behavior [7]. These optogenetically induced behaviors resemble the reactions of mice to
49 visual stimuli that mimic avian predators [19,20]. These experiments suggest that activation of
50 neurons early in the visuo-motor circuits of the SC leads to downstream activity and behaviors
51 that are comparable to the network activity and behaviors triggered by natural visual stimuli.
52 But our view of these circuits remains limited to the specific circuits that have been
53 investigated to date.

54 In rodents, combinations of cell-type specific stimulation and whole brain recordings using
55 functional magnetic resonance imaging (fMRI) have provided insights into the relationship
56 between cell-types and brain-wide network activity [21,22]. In relation to the SC, fMRI studies in
57 humans have provided evidence that the pathway linking the SC to the amygdala (AMG) via
58 LP is involved in the processing of visual threats [23–25]. However, recording techniques such as
59 fMRI suffer from limited resolution, which makes it difficult to clearly assign activity to small
60 brain nuclei, in particular in small mammals [21,26]. Functional ultrasound imaging (fUSi) has been
61 developed to study brain-wide activation patterns at a spatial and temporal resolution in awake
62 mice that makes it practical to follow neural activity in most nuclei of the brain at a resolution
63 of ~100 μm [27–32]. In addition, its compact size allows for parallel interventions such as
64 optogenetic activation or local neuronal recordings in awake behaving animals [31,33].

65 By combining fUSi with optogenetics (opto-fUSi), we reveal in this study the neural networks
66 through which information is routed after activation of different cell-types in the SC. We unravel
67 the differences in the spatial and temporal organization of network activation depending on

68 the cell-type and link these to differences in evoked behaviors. Opto-fUSi allows us to identify
69 new brain areas that link sensory inputs to behavioral output, and we demonstrate that these
70 brain areas are also activated by threat-like visual stimuli. Finally, chemogenetic manipulations
71 unravel the potential function of one newly identified group of nuclei, the posterior paralaminar
72 nuclei of the thalamus (PPnT), in visually triggered aversive behaviors.

73 **Results**

74 **Different collicular cell-types trigger different defensive behaviors**

75 To understand the contributions of different collicular cell classes to defensive behaviors, we
76 optogenetically manipulated the activity of four genetically defined cell populations:
77 1) a population of excitatory neurons expressing CAMKII, referred to as CAMKII; 2) NTSR
78 neurons that project to the LP, referred to as NTSR [13]; 3) the population of parvalbumin
79 expressing neurons (PV) that consists of local interneurons and excitatory projections to LP,
80 PBG and pontine gray (PG); 4) a set of inhibitory neurons (GAD2) that innervates the lateral
81 geniculate nucleus (LGN) and PBG [13]. We restricted the expression of light-sensitive
82 channelrhodopsin2 (ChR2) to the distinct cell classes in two ways. First, to express ChR2 in
83 NTSR, PV and GAD2 neurons, we crossed Cre-expressing transgenic mouse lines (NTSR-
84 GN209-Cre, PV-Cre and GAD2-Cre) with a ChR2-reporter mouse line, Ai32 [34–37]. Second,
85 CAMKII neurons were labeled with an adeno-associated virus (AAV) that carried ChR2 under
86 the CAMKII promotor [17] (see Methods). Control experiments were carried out with Cre-
87 negative litter mates. Histological analysis confirmed the layer-specific expression of ChR2 in
88 different cell-types (Figure 1B), which was consistent with previous reports [6–8,12,13,17].

89 To optically stimulate the colliculus, we stereotaxically placed an optical fiber over the medial
90 portion of the superficial layers (Figure S1F). We performed the behavioral experiments in an
91 open field setup (50 cm x 50 cm box). At the beginning of each session mice were given a
92 minimum of 2 minutes to freely explore the box before the experiments began (Figure 1A).
93 Typically, animals were found to actively explore the box soon after being released into the
94 arena, regularly moving from one corner to another (Movie S1; all the movies are listed an
95 described in Table S1). Each trial was initiated when an animal entered the center of the arena,
96 at which point we manually triggered the optogenetic stimulation. The stimulus consisted of
97 blue light pulses (473 nm, 2 ms pulse width, ~9.5 – 12.5 mW/mm^2) of either 1 s duration at 20
98 or 50 Hz or 4 s duration at 5 Hz. CAMKII and NTSR neurons were stimulated at 20 Hz, whereas
99 GAD2 and PV neurons at 50 Hz. We chose the stimulation frequency based on our preliminary
100 behavioral observations (see Methods), and the documented firing rates recorded in response
101 to natural visual stimuli [6–8,13,17,38]. We obtained similar results using either a 20 or 50 Hz (Figure
102 1) or 5 Hz (Figure S1A-F) stimulus. In the following paragraphs we focus on data obtained
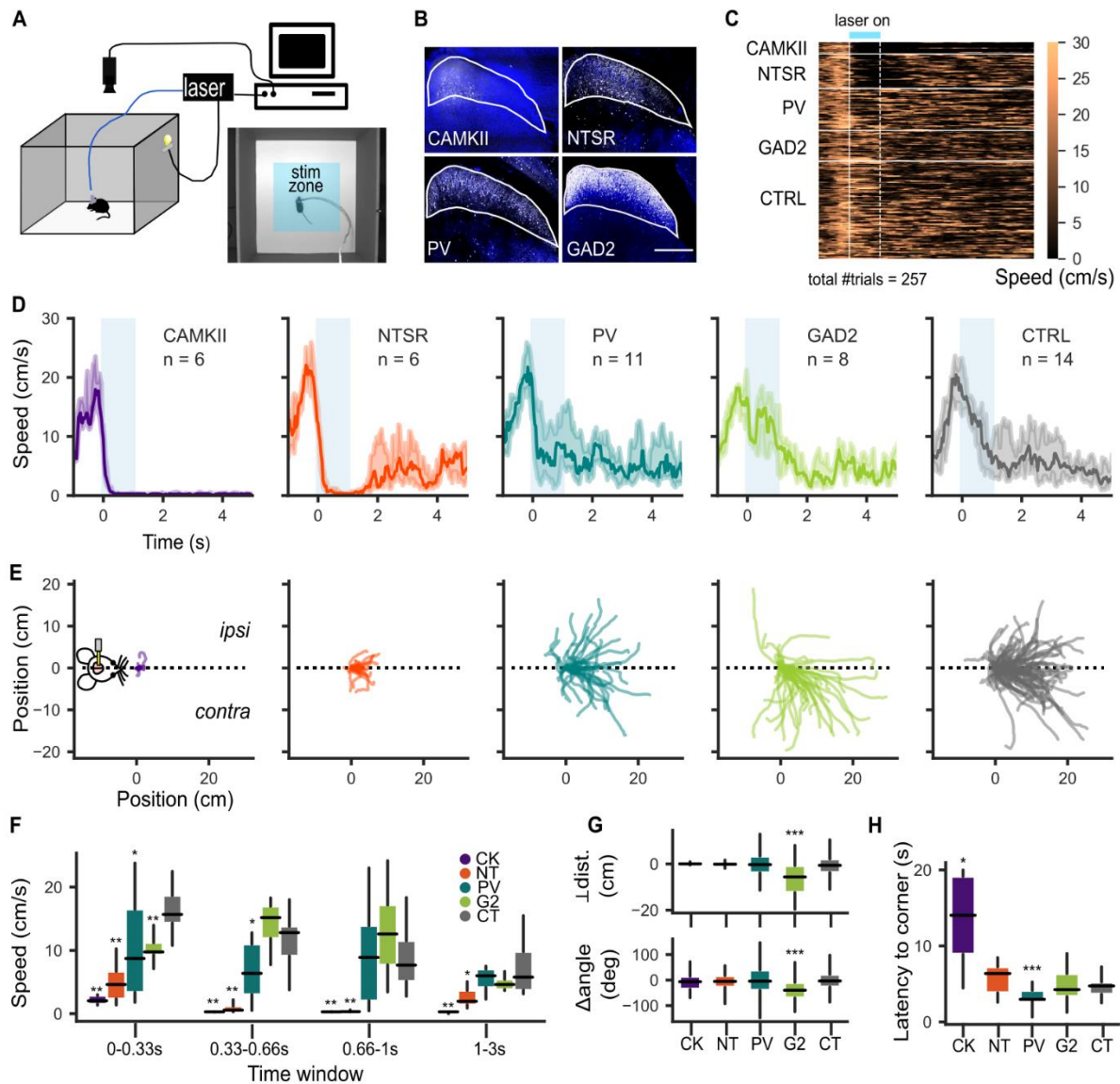103 using the 20 or 50 Hz 1 s stimulus.

4

Figure 1. Different SC cell-types trigger different defensive behaviors. A. Schematic diagram of the open field setup for optogenetics and a video frame of mouse entering the stimulation zone in the center of the box (bottom right, stimulation zone is marked with blue rectangular shading). **B.** Coronal section showing expression of ChR2 in distinct cell lines. Scale bar, 500 μm. **C.** Heatmap of mice speeds during optogenetic stimulation trials. Values were obtained from the first experimental session for each animal. Horizontal white lines separate different mouse groups. Vertical solid and dashed white lines mark stimulus onset and offset, respectively. Light blue bar on the top marks the stimulus duration. **D.** Speed profiles. Each trace represents the median speed obtained from each mouse line. Shaded area represents the interquartile range. **E.** Mice trajectories during the stimulus duration (1s). Traces were aligned and rotated by the initial body position angle. CAMKII: n=6, 14 trials, NTSR: n=6, 41 trials, PV: n=11, 50 trials; GAD2: n=8, 43 trials; CTRL n=8, 77 trials. **F.** Speed quantification during chosen time windows. (0-0.33s: CAMKII p=0.0003, NTSR p=0.0003, PV p=0.026, GAD2 p=0.004; 0.33-0.66s: CAMKII p=0.0003, NTSR p=0.0004, PV p=0.03, GAD2 p=0.10; 0.66-1s: CAMKII p=0.003, NTSR p=0.0004, PV p=0.34, GAD2 p=0.10; 1-3s: CAMKII p=0.0003, NTSR p=0.007, PV p=0.38, GAD2 p=0.18) **G.** Quantification of preferred body position at the stimulation offset, represented as a change of angle (bottom; CAMKII p=0.26; NTSR p=0.31; PV p=0.45; GAD2 p=0.00002) and perpendicular distance (top; CAMKII p=0.27; NTSR p=0.29; PV p=0.38; GAD2 p=0.00002), both in reference to X axis (dashed line in E). **H.** Quantification of latency to a corner (CAMKII p=0.003; NTSR p=0.15; PV p=0.013; GAD2 p=0.49). All data points are averaged over mice, except in G where the data points are averaged over trials. Significance between control and each mouse line was tested using Mann-Whitney U-test (alpha = 0.05). Box-and-whisker plots for F-H show median, interquartile range and range. * p <0.05, ** p <0.01, *** p <0.001.

104

5

105 Activation of each neural population led to distinct behavioral responses, that ranged from
106 stopping (CAMKII and NTSR neurons) to directed movement (PV and GAD2 neurons; Figure
107 1). To capture differences in the triggered behavior, we first looked at the speed dynamics
108 (Figure 1C-D and Figure 1F). All experimental groups responded with a drop in speed during
109 the first 333 ms following the start of the stimulation (Figure 1F; Mann-Whitney U-test
110 compared with control, CAMKII: p=0.0003; NTSR1: p=0.0003; PV: p=0.026; GAD2: p=0.004),
111 whereas control mice did not show any identifiable change in behavior (Movie S2). An animal
112 was determined to have stopped if its speed dropped below 1.5 cm/s for at least 0.5 s.
113 Activation of CAMKII neurons resulted in particularly long stopping events that lasted for up to
114 19.8 s (Figure S1H, Movie S3; median stopping duration: 9.21 s, IQR=[8.02, 12.65]),
115 whereas stimulation of NTSR neurons resulted in mice stopping during the 1 s stimulus and
116 resuming locomotion shortly after stimulus offset (median stopping duration 1.69 s, IQR=[1.42,
117 1.95]; Figure S1H, Movie S4). Activation of PV cells caused mice to slow down, but rarely led
118 to a full stop (Figure S1I). Instead, their behavior was characterized by active movement
119 towards one of the corners (Figure 1H, Movie S5; median latency: 2.96 s, IQR=[2.7, 4.16];
120 Mann-Whitney U-test compared with control, p=0.01). Animals with ChR2 expression in GAD2
121 neurons showed a tendency to increase their speed during the stimulation (Figure 1F; Mann-
122 Whitney U-test compared with control, GAD2: p=0.10). Interestingly, this was accompanied by
123 movement contralateral to the stimulated hemisphere (Figure 1F-G) that manifested itself as
124 turning (Movie S6, Figure 1G Bottom, median Δ angle: -39°, IQR=[-70.01, -9.36]; Mann-Whitney
125 U-test compared with control, GAD2: p=0.00002), or a whole-body drift quantified as the
126 perpendicular to the distance traveled in the first second relative to the axis of motion before
127 the stimulus (Movie S7, Figure 1G Top; median perpendicular distance: -5.66 cm, IQR=[-
128 12.36,-0.72]; Mann-Whitney U-test compared with control, GAD2: p=0.00002). Taken together,
129 these findings suggest that each collicular cell-type makes a different contribution to behavior
130 that can broadly be characterized as defensive or orienting.

131 **Brain-wide functional ultrasound during optogenetic stimulation in mice**
132 In order to assess the brain-wide neural activity that drives the different behaviors observed
133 above, we developed a chronic preparation that allowed us to combine functional ultrasound
134 brain imaging (fUSi) and optogenetics, in awake head fixed animals (Figure 2, A-C). fUSi
135 reports neuronal activity indirectly by measuring changes in blood volume of the
136 microvasculature [32,39,40]. To accommodate the optogenetic fiber and image as much of the
137 brain as possible, a large cranial window that spanned a single hemisphere was implanted (AP
138 +2 to -6.5; L +1.25 to -4.5). An optic fiber was pointed at the surface of the ipsilateral SC near
139 the midline at an angle of 56°, approached from the contralateral side (Figure 2B; Methods). All
140 animals included in the fUSi experiments were tested for behavior before each imaging
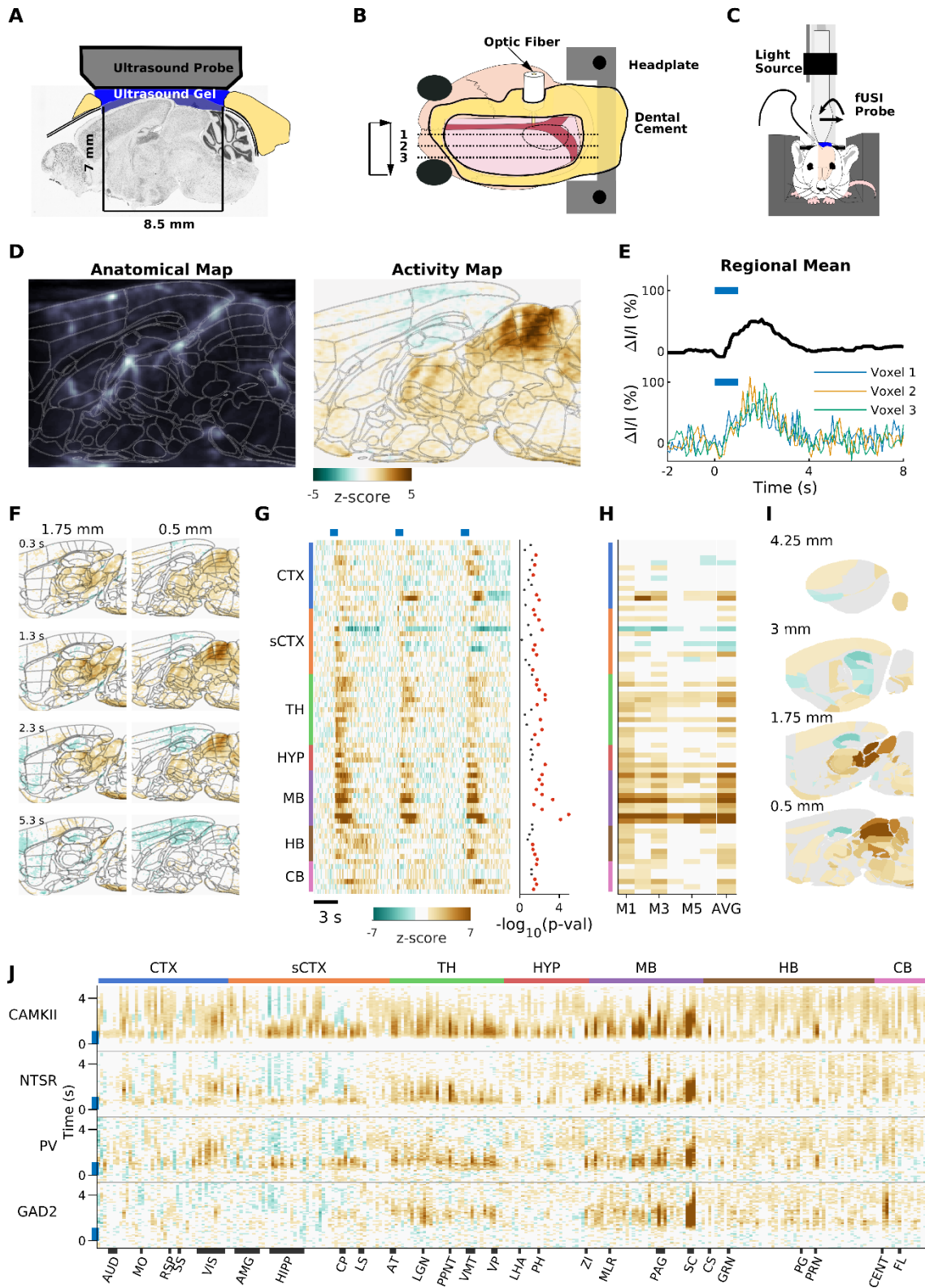141 session.

142

143

Figure 2. Functional ultrasound imaging of awake mice during optogenetic stimulation. A. Scheme of a sagittal cross-section of the chronic preparation. **B.** Top-view scheme of a chronic cranial window with implanted optic-fiber cannula inserted at 56 º. **C.** Schematic of experimental set-up for awake imaging. **D.** Left. Example sagittal section of a blood volume map registered to the Allen Mouse brain reference atlas (thin gray lines). Right. Voxel to voxel normalized response to optogenetic stimulation of plane shown in left panel, registered to the Allen Mouse brain reference atlas (thin gray lines). **E.** Bottom: relative hemodynamic response curves to the optogenetic stimulation of three example voxels in the intermediate superior colliculus. Top: mean response of the intermediate superior colliculus. Blue lines indicate duration of optogenetic stimulation. **F.** Two example sagittal planes from the activity maps of a single animal. **G.** Left: Standardized responses of a selection of 72/264 segmented areas. Mean responses are shown for 3 different mice. Response for each mouse is an average of 6 trials. Blue lines indicate duration of optogenetic stimulation. black thick line indicates optogenetic stimulation. Right: Inactive (gray) and active (red) areas colored based on significance threshold corrected for multiple comparisons (p<0.05). **H.** Mean response of each segmented area shown in G during the 2 s after the start of the stimulus for 6 different NTSR mice and the average across all mice. Areas considered not significant (p>0.05) are set to zero in the average. **I.** Projection of the average activity vector from H onto a map of the mouse brain. **J.** Average time course of each of the 264 segmented areas for each stimulated cell population. Black bars along the bottom indicate span of the labeled brain regions.

CTX: cortex, sCTX: cortical subplate, TH: thalamus, HYP: hypothalamus, MB: midbrain, HB: hindbrain, CB: cerebellum

AUD: Auditory cortex, MO: Motor cortex, RSP: Retrosplenial cortex, SS: Somatosensory cortex, VIS: Visual cortex, AMG: Amygdala complex, HIPP: Hippocampus, CP: Caudatoputamen, LS: Lateral septum, AT: Anterior thalamus, LGN: Lateral geniculate nucleus, VMT: Ventromedial thalamus, VP: Ventral posterior thalamus, LHA: Lateral hypothalamic area, PH: Posterior hypothalamic area, ZI: Zona incerta, MLR: Mesencephalic locomotor region, CS: Superior central nucleus raphe, GRN: Gigantocellular reticular nucleus, PG: Pontine gray, PRN: Pontine reticular nuclei, CENT: Cerebellar lobuli, FL: Flocculus

144   Neural activity was monitored with a fUSi probe positioned over the craniotomy parallel to the
145   long axis of the animal. Sagittal planes were imaged sequentially, each spanning the entire
146   depth of the brain, where the probe was stepped (250 um) along the medial-lateral axis (Figure
147   2A-C). While imaging each plane, the colliculus was optically stimulated. In each experiment,
148   each plane was imaged for two 20 s periods, when either a 1 s (20 Hz or 50 Hz), or 4 s (5 Hz)
149   light stimulation was delivered via the implanted optic fiber 10 s after the imaging started. The
150   parameters of the light stimulation were the same as those used during the behavioral
151   experiments. Each mouse was imaged in 3-5 sessions that were separated by 48-72
152   hours. Each voxel was assigned to an individual brain region by performing a 3D rigid
153   registration of the series of sagittal images, obtained in the absence of visual stimulation (125
154   µm steps), to the Allen Mouse Brain Common Coordinate Framework version 3 (CCF v3) [41]
155   (Figure 2D). We used a modified version that is comprised of 264 brain areas in one
156   hemisphere of the brain (Table S2).

157   To build a spatial map of brain activity, we compared, voxel by voxel, the hemodynamic signals
158   (DI/I, referred to as "activity") obtained during and after the optogenetic stimulus to a 10 s
159   period before the light stimulus (Figure 2D-F; Movie S8). The hemodynamic activity of all
160   voxels within each area were averaged to estimate the response for that region (Figure 1E and
161   G). Temporal traces were obtained for each mouse and compared (t-test corrected for false
162   discovery rate) to identify the areas that displayed a response (Figure 1G, H-I). Average
163   responses for each segmented area in each mouse line are shown in Figure 1J. The same
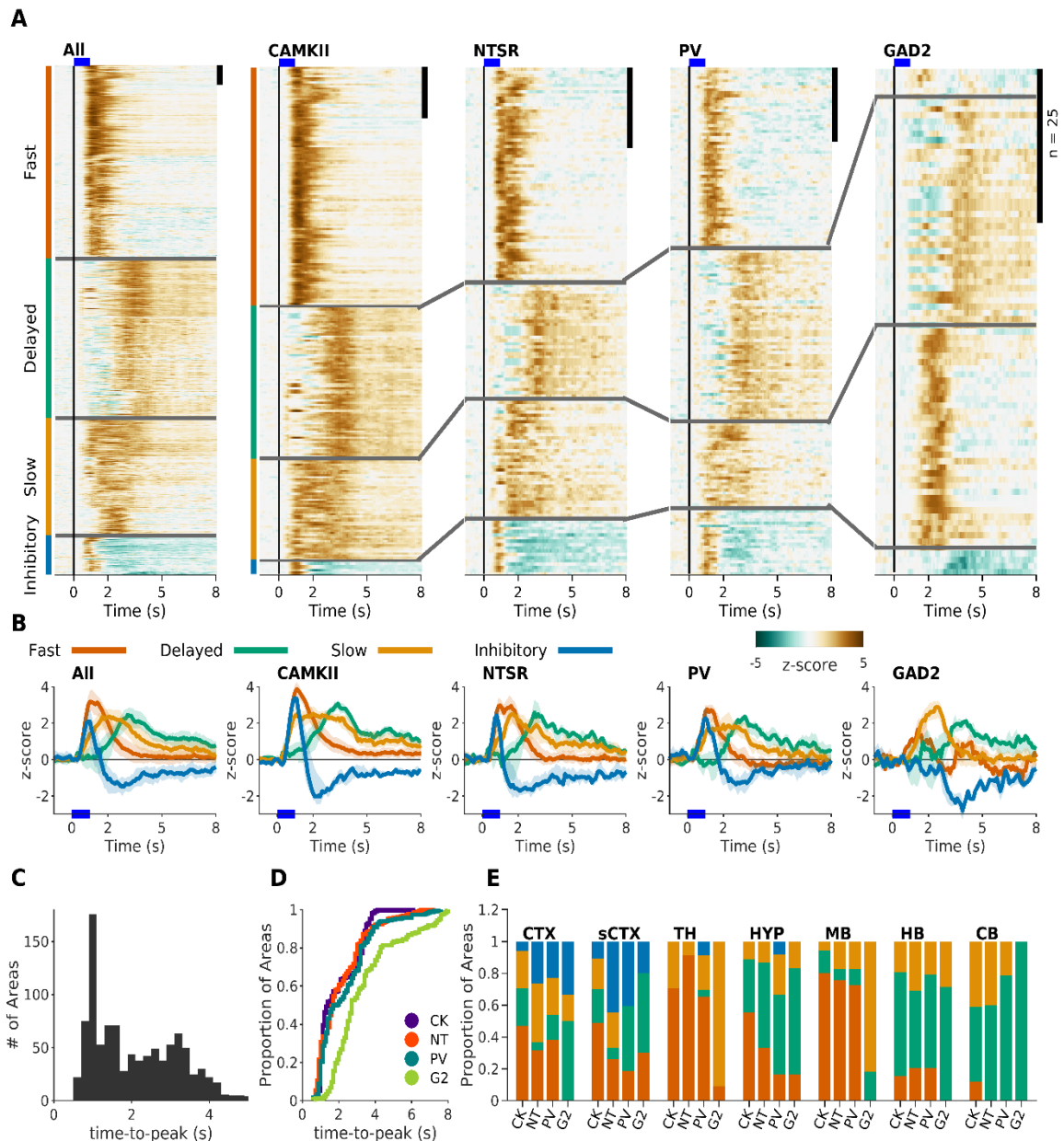164   analysis was applied to low-frequency stimulation data (Figure S3).

Figure 3 Distribution of temporal responses dynamics. A. Normalized responses to optic stimulation. Responses are organized into their respective clusters: Fast (orange), Delayed (green), Slow (yellow) and Inhibitory (blue). Black scale bar at top right of each panel represents 25 areas. Blue line represents the 1 s optical stimulus. Left Panel. Responses of all areas that had a statistically significant response across all cell populations (n = 659). Other panels are the active areas in each mouse line (CK = 246, NT = 157, PV = 170, G2 = 82). **B.** Average response of each of clustered responses. **C.** Histogram of the time-to-peak of each active area in all mouse lines. **D.** Cumulative histogram of time-to-peak in each mouse line. **E.** Proportion of each response type sorted by brain area and mouse line.

Distribution of temporal response properties

We began our analysis of how distinct cell-types of the SC distribute information across the brain by looking at the temporal structure of the hemodynamic changes induced by the optical stimulation (Figure 3). We found that our 1 s optical stimulus caused a reliable set of temporal responses that could be grouped into 4 broad categories (see Methods). These four response types could be broadly described as: Fast, Delayed, Slow and Inhibitory (Figure 3A and B). The Fast responses were characterized by a relatively fast rise time (1.27 +/- 0.42 s), resulting in a transient response. The Delayed responses showed a clear delay with time to peak of 3.3

9

173   +/- 0.79 s. The Slow responding areas started their responses early but took longer to reach
174   their peak (2.1 s +/- 0.70 s) and showed a more sustained response (1.78 +/- 1.30 s). Finally,
175   a set of responses that we will refer to as Inhibitory, showed a negative response. Inhibitory
176   responses were commonly preceded by a very transient early positive response (time-to-
177   peak = 0.91 +/- 0.65 s: decay time = 0.52 +/- 0.18 s) in each cell-class except the GAD2 (Figure
178   3A and 3B).

179   The distribution of the different response types varied among the mouse lines. We found that
180   the Fast responses were more common in CAMKII and NTSR mice (CK 47%; NT 42%; PV
181   35%; G2 5%). PV mice had a similar proportion of fast (35%) and delayed (34%) responses,
182   while GAD2 mice had predominantly delayed (45%) and slow (44%) responses. In addition,
183   inhibitory response types were more common in NTSR and PV mice, as compared to CAMKII
184   and GAD2 (CK 3%; NT 11%; PV 13%; G2 5%). The almost complete absence of Fast responses
185   in the GAD2 mice is evident in the distribution of the response latencies, estimated as the time-
186   to-peak (Figure 3C-D). The distribution of latencies formed two broad groups, those
187   responding within the first 2 s, and those responding after 2 s (Figure 3C). While the distribution
188   of latencies is similar for CAMKII, NTSR and PV cell populations, and spanned the entire range
189   of times, activation of inhibitory GAD2 neurons did not cause any early responses (Figure 3A
190   and 3D).

191   Stimulating the SC neurons at a lower frequency (5 Hz for 4 s), generated similar temporal
192   dynamics triggered by each neuronal population (fast, delayed, slow, inhibitory), but
193   exacerbated the differences between them (Figure S3). Additionally, the change in frequency
194   corresponded with a reversal in the sign of the response in some areas such as the visual
195   cortex. The visual cortex had a fast positive response during high-frequency stimulus, but an
196   inhibitory response during the low-frequency for each cell population (Figure 3 and Figure S3).

197   The distribution of the different response types across the major brain structures was relatively
198   consistent between the different cell populations, except for slow responses (Figure 3E). Fast
199   responses occurred mainly in the midbrain and thalamus, delayed activations took place in
200   hypothalamus, hindbrain and cerebellum, and inhibitory responses in the cortex and cortical
201   subplate. Slow responses were more homogeneously distributed. For example, CAMKII and
202   NTSR had the largest proportion of slow responding areas in the cerebellum (23 and 24%,
203   respectively), while GAD2 had none in that structure.

204   **Different brain-wide activity patterns are triggered by each class of cells**
205   To understand how the activation of each neuronal population triggers distinct brain-wide
206   networks, we compared the distribution of brain areas that had increased or decreased
207   hemodynamic responses for each cell-type. Based on the temporal dynamics of the
208   responses observed (Figure 3C), we performed this comparison in two distinct time windows,
209   an early (0-2 s) and a late (3-8 s) phase (Figure 4A). Complete lists of the responsive areas to
210   high- and low-frequency stimuli are provided in the supplementary materials (Table S3-S4).
211   3D movies of the activated brain areas can be found in the supplementary material for the
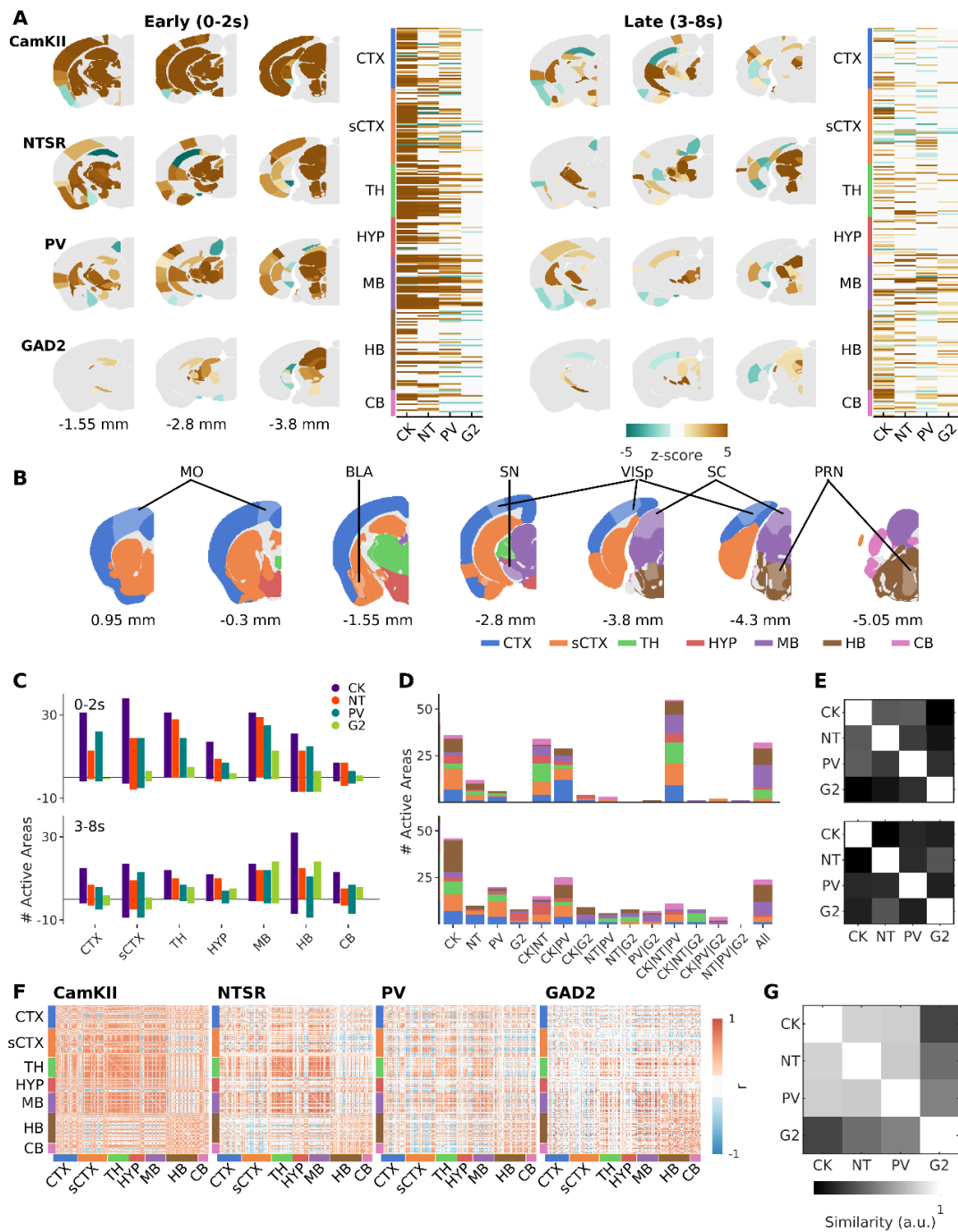212   early (Movie S9-12) and late phase (Movie S13-16).

213

Figure 4. Cell-type specific activation of downstream pathways of the superior colliculus. A. Activation maps during early (Left, 0-2 sec) and late (Right, 3-8 sec) time windows. Three example coronal slices are shown for each mouse line. Active areas are shown in each plane with the mean z-score across mice (CK=6; NT=6; PV=13; G2=6). Next to the activation maps, is the peak response of all areas active in at least one mouse line. **B.** Summary of the extent of the imaging locations and corresponding names. Imaging was done in 264 brain regions. Here we delineate the major brain areas and highlight a few single regions for orientation. A complete list of the segmented brain regions and abbreviations are presented in Table S2. **C.** Distribution of active areas during early and late phases. **D.** Quantification of shared areas across mouse lines during early (Top) and late (Bottom) phases. Areas included in one group are excluded from the others. **E.** Similarity matrix (between cell populations) of maximum activity during early (Top) and late (Bottom) phases. **F.** Pairwise Pearson correlation coefficients between the mean response traces of the 264 segmented areas during the 8 s after stimulus onset. **G.** Similarity between the correlated hemodynamic responses in F.

11

214   The distribution of responsive areas across the brain in the early and late phases followed
215   different patterns for each of the cell classes (Figure 4A and C). Broadly, stimulating CAMKII,
216   NTSR and PV cell-types at high-frequency, resulted in more responses during the early phase
217   (CK=193; NT=138; PV=129), as compared to the late phase (CK=142; NT=82; PV=97). In
218   contrast, stimulating GAD2 cells resulted in 41 areas responding during the first two seconds,
219   followed by an additional 68 areas responding during the late phase. When we compared the
220   distributions of the active areas (Figure 4C), we found that stimulation of CAMKII evoked
221   responses in large portions of the CTX (80%, 33/41 areas), sCTX (80%, 41/51 areas), TH (80%,
222   31/36 areas) and MB (89%, 33/37 areas) in the early phase, but was dominated by HB (72%,
223   39/54 areas) and CB (79%, 15/19 areas) in the late phase. Stimulating the NTSR population
224   activated large portions of the MB (78%), and TH (78%), during the early phase (other
225   structures ranged from 34%-58%) and had less but more distributed activity during the late
226   phase (CTX: 24%, sCTX: 27%, TH: 28%, HY: 38%, MB: 41%, HB: 28%, CB: 42%). PV neurons
227   preferentially modulated the MB (MB: 70%; others: 31-59%) in the early phase, and the HB
228   (HB: 74%; others: 22-43%) in the late phase. In GAD2 mice, most areas were activated in the
229   MB in the early phase (MB: 38%; others: 2-19%). During the late phase, GAD2 activated more
230   areas across the whole brain, particularly in the MB (early/late; 38% / 54%), the HB (early/late;
231   19% / 33%) and CB (early/late; 16% / 32%). Low-frequency stimulation did not change the
232   overall distribution of responsive areas in early and late phases of the different cell-types
233   (Figure S4A). However, compared to high-frequency, PV and GAD2 mice had a noticeable
234   decrease of activated areas in both the early (high-frequency/low-frequency; PV: 129/72;
235   GAD2: 41/14) and late (high-frequency/low-frequency; PV: 97/73; GAD2: 68/9) phases.
236   Differently, NTSR mice had more responsive areas in both early and late phases, most
237   noticeable in the HB during the late phase (high-frequency/low-frequency; HB: 28% / 93%). Of
238   note, the early phase of NTSR mice had a large increase of negatively modulated areas of the
239   cortex by low-frequency stimulation, which had positive responses upon high-frequency
240   stimulation (Figure S4A-B).

241   To gain insight into the different downstream networks, we next looked at the overlap between
242   the areas modulated by the different cell classes (Figure 4D-E). We found that in the early
243   phase up to 93 areas had shared activity between at least three of the neuronal populations,
244   71 where shared by only two, and 54 areas were unique. Consistent with the fact that the
245   CAMKII population likely includes the other two excitatory cell-types, when two areas were
246   shared, in most cases it was between CAMKII and either PV (29) or NTSR (34) mice. During
247   the late phase, the specificity increased and only 47 areas where shared by three or more cell-
248   types, compared to the ones shared by two (70) or uniquely modulated (84). To measure how
249   similar the activated networks were from each other, we calculated the similarity between cell-
250   lines of the maximum activity during early and late phases (Figure 4E). We found that during
251   the early phase, the greatest similarity was between PV and NTSR with CAMKII (Figure 4E).
252   GAD2 showed the least similarity with the other cell lines. During the late phase, GAD2 and
253   NTSR mice showed the highest similarity towards each other (Figure 4E Bottom), and all other
254   pairings showed very low similarity. Low-frequency stimulation was characterized by a large

255 increase in the number of areas solely activated by NTSR neurons (Figure S4E). Similarity
256 analysis showed that, in the early phase, CAMKII and PV networks were the most similar
257 (Figure S4D Top). In the late phase, the similarity pattern was conserved, with GAD2 and NTSR
258 networks being the most similar (Figure S4D Bottom).

259 Finally, in order to compare the activated networks from a holistic point of view, we generated
260 functional connectivity maps of the relationship between areas across the whole brain (Figure
261 4F). To do this, we first quantified the pairwise correlation across all active areas of each
262 neuronal population. Then, we compared the resulting matrices to each other (Figure
263 4G). Broadly, correlations across the brain upon high-frequency stimulation followed similar
264 patterns in CAMKII, NTSR and PV, and were clearly different from GAD2. More concretely,
265 CAMKII, NTSR and PV mice all had a marked high level of correlation between areas of the
266 MB and TH. In GAD2 the highest correlations where between the MB, the HB and the CB.
267 Under low-frequency stimulation, CAMKII and NTSR mice continued to have similar correlation
268 patterns across the brain (Figure S4E-F), but there was a pronounced shift of the brain-wide
269 correlations that showed increased correlations of the MB with the HY, HB and CB and a
270 decrease with CTX and sCTX. The change in frequency did not affect the brain-wide
271 correlations of PV mice, while the correlations for GAD2 became sparser and more localized
272 within the different structures, making it the most differentiated cell-type (Figure S4F). Taken
273 together, these results indicate that each collicular cell-type modulates a distinct brain-wide
274 network.

275 **Defensive and fear related networks are differentially modulated by each cell class.**
276 To understand how the activation of each neuronal population triggers distinct aversive
277 behaviors, we compared the activity patterns of each cell-type within a list of 30 areas that
278 have been previously shown to mediate or modulate defensive behaviors (Figure 5A). This
279 comparison showed that each neuronal population activated a different subset of areas or
280 modulated the same areas in a different manner. For example, the central amygdala (CEA),
281 the posterior medial and paraventricular hypothalamic areas (PMH, PVH), and the ventral
282 tegmental area (VTA) were shared uniquely by cell classes that elicited freezing-like behaviors
283 (CK, NT). On the contrary, the cuneiform (CUN), or the superior central nucleus (CS) were
284 activated by all mouse lines but exhibited different temporal dynamics. The CUN had fast
285 transient responses in CAMKII and NTSR and slower sustained responses in PV and GAD2
286 mice, whereas the CS had sustained responses in CAMKII and GAD2 but transient in NTSR
287 and PV. Interestingly, there were also cases where different cell-types activated the same
288 areas but in opposite directions. For example, areas of the ventral midline thalamus (RE and
289 Xi), cingulate cortex (ACAd), and subthalamic nucleus (STN), had positive responses to
290 CAMKII and NTSR types, but were dominated by negative responses in PV. Finally, a few areas
291 were similarly activated by all mouse lines, namely the motor layers of the colliculus (SCi), the
292 dorsal periaqueductal gray (PAGd) and the zona incerta (ZI), all with similar fast positive
293 responses. When we compared the correlated activity across this group of areas (Figure 5B),
294 and the similarity of the traces (Figure 5C) across the different mouse lines, it confirmed that
295 CAMKII and NTSR evoked the most similar responses compared to PV, and GAD2. Principal
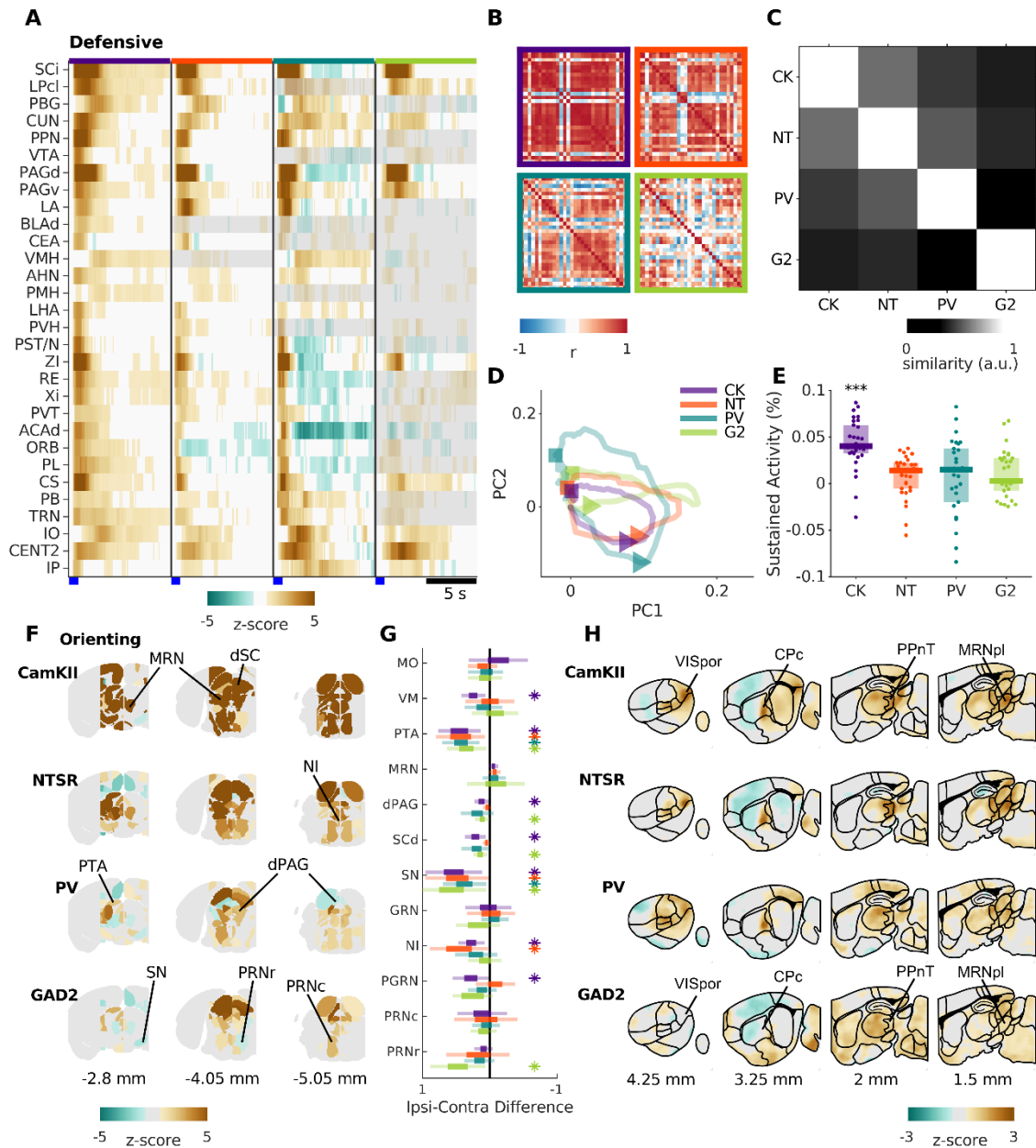
Figure 5. Activity in behaviorally defined networks. A. Heatmap of the average responses of 30 nuclei commonly associated with defensive behaviors triggered the different cell populations. **B.** Correlation matrix of the responses in each cell populations. **C.** Similarity of the response properties of these 30 areas across cell populations. **D.** 2D Trajectories of the neuronal activity in these 30 brain areas. Triangle and square are the points on the trajectories 1.5 s and 5 s after the stimulus, respectively. **E.** The average sustained activity for each of the 30 areas after high-frequency stimulus of each cell population. Each dot represents a brain area. **F.** Comparison of the activity in the nuclei that lie within 2 mm of the midline, both ipsi- and contralateral to the optogenetic fiber stimulus. Each ipsi-contra pair is shown when the difference is the highest within a 4 s window after stimulus onset **G.** The percent difference in the fUSi signal between the ipsi- and contralateral brain areas. * represent differences that were statistically significant (p < 0.05 permutation test, after correction for multiple comparisons). Light color lines represent the estimated 95% confidence intervals. Dark portions represent the interquartile range. **H.** Average pixel-pixel maps of four sagittal sections from each neuronal population that highlight brain areas not commonly reported to mediate visually guided defensive behaviors.

296

297

14

298 component analysis of the trajectories followed by the responses (Figure 5D), showed that
299 CAMKII and NTSR evoked almost identical responses during the first 2 seconds after the
300 stimulus onset, but then diverged into different paths. This was likely due to the more sustained
301 activity evoked by the excitation of CAMKII neurons (Figure 5E). These results are consistent
302 with the different collicular cell-types activating distinct behaviors through parallel functional
303 networks.

304 **Asymmetric activity originating from the medial part of the superior colliculus**
305 Orienting behaviors, including eye, head and body movements can be controlled via
306 contralateral projections of the SC to the medial pontomedullary reticular formation (MPRF)
307 [42,43]. In mice the MPRF is comprised of a set of nuclei that includes the pontine gray and pontine
308 reticular nuclei (PRN) that we were able monitor on both sides of the brain as they lie close to
309 the midline. On the contrary, defensive behaviors are thought to be mediated mainly by
310 ipsilateral pathways originating in the medial part of the SC [44]. Consistent with our stimulations
311 targeting the medial part of the colliculus, we found that all cell-lines evoked asymmetric
312 activations that where preferentially ipsilateral (Figure 5F-G). Also, activating GAD2 neurons
313 generated the greatest number of asymmetries, including pontine areas such as the rostral
314 part of the PRN, which is in line with that cell line being the only one triggering a change in
315 orientation.

316 **Novel areas involved in collicular-driven aversive behaviors**
317 Visual inspection of brain-wide activity maps (Figure 5H), revealed a few highly responsive
318 nodes in areas that have not been previously studied in the context of collicular-driven
319 defensive behaviors. The four areas that were most salient were the the caudoputamen,
320 especially its caudal part (CPc); the postrhinal visual area (VISpor); the posterior lateral part of
321 the midbrain reticular formation (MRNpl) and a group of thalamic areas surrounding the medial
322 geniculate complex referred to here as the posterior paralaminar nuclei of the thalamus (PPnT)
323 [45]. The VISpor and CPc are known di-synaptic targets of the colliculus, via the pulvinar, but
324 have not been implicated in guiding defensive behaviors [46–49]. The MRNpl and PPnT have not
325 been previously described to receive mono- or di-synaptic inputs from retino-recipient
326 neurons of the SC [14].

327 **Correspondence between fUSi and neuronal activity**
328 To test to what degree fUSi signals correlate with the underlying spiking activity, we used
329 Neuropixels probes to record from different parts of the brain and compare them to the fUSi
330 responses observed for the same stimulus. We focused on NTSR cell population in Ntsr-Cre x
331 Chr2 mice. Animals were head-fixed on a treadmill or floating ball and neural activity was
332 recorded while either optogenetically activating NTSR neurons with repeated trials of 1 s 20 Hz
333 stimulation, or while viewing visual stimuli on a screen (Figure 6A). The recording probes were
334 coated with a fluorescent dye (DiI) to visualize the recording locations post-hoc (Figure 6B). On
335 some electrodes, we found spiking activity that was triggered by each of the 20 light pulses
336 (Figure 6C Top). On other electrodes, while the response to the first light pulse was often
337 strong, the responses to the subsequent pulses were weak or absent (Figure 6C middle and
338 Bottom). A raster plot of all 384 recording electrodes for one trial of 20 light pulses are shown
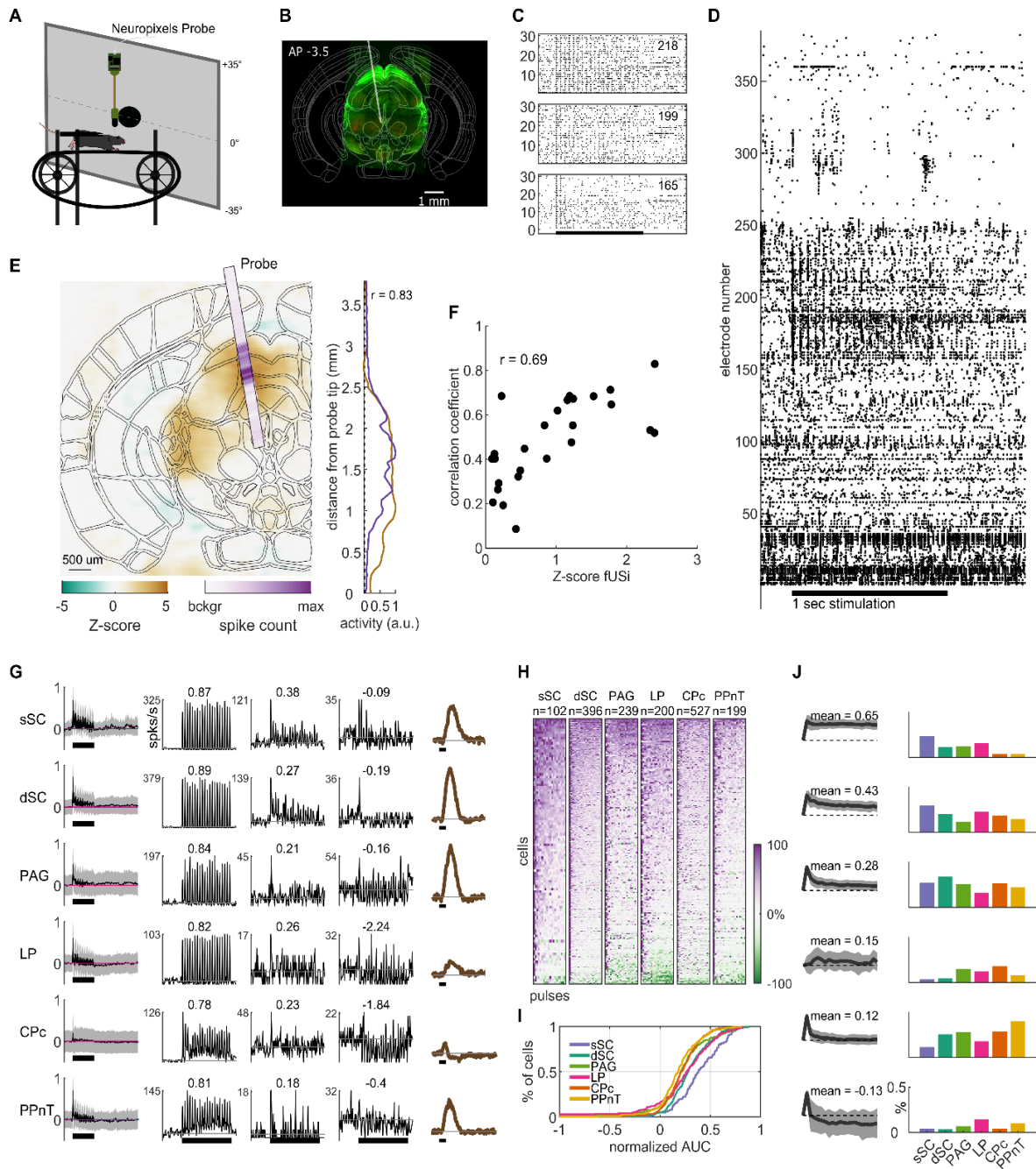
15

339

Figure 6. Correspondence of fUSi and spiking activity. A. Setup for Neuropixels recordings in awake, head-fixed mice. **B.** Example histological section with Ntsr-Chr2 positive neurons (green) and the probe location indicated with a gray line. **C.** Raster of spikes for 30 repetitions of the optogenetic stimulus for three example electrodes. Stimulus time (1 s, 20 pulses) is indicated with a black bar. **D.** Raw spiking data on all 384 electrodes of the probe shown in B during a 20 Hz optogenetic stimulation of NTSR neurons. **E.** Overlay of fUSi and spiking activity for a colliculus recording. r indicates correlation coefficient of the average activity on the probe and the corresponding pixels of the fUSi data. **F.** Dependence of correlation between fUSi and probe recordings on overall fUSi response strength. **G.** Average response (averaged across all optogenetic stimuli, background-subtracted and normalized) of sorted units in six selected areas (Left; mean ± std). Responses to optogenetic stimulation of 3 example cells for each area. The cell with the highest area under the curve (AUC) (second column), the medium AUC (third column) and the lowest AUC (fourth column) as well as the temporal fUSi response (last column). Numbers indicate AUC. **H.** Response strength to each optogenetic pulse sorted by AUC. 0% is background activity. **I.** Cumulative distribution of AUCs for each area. **J.** Responses to the 20 optogenetic pulses were clustered into 6 types. Average and STD of the normalized response strength for each cluster as well as average AUC (left) and % of cells for each response type and area (Right).

sSC - superficial superior colliculus; dSC - deep superior colliculus; PAG - periaqueductal gray; LP - lateral posterior nucleus of the thalamus (pulvinar); CPc - caudate putamen; PPnT - posterior paralaminar nuclei of the thalamus.

16

340   for a penetration (from Figure 6B) that passed through the cortex, the SC and periaqueductal

341   gray (Figure 6D). Spikes were defined as local peaks of 4 times the standard deviation of the

342   average activity before stimulation. Detected maxima during the 1 ms pulse itself were

343   excluded since they were contaminated by electrical artifacts (see Methods). Clear responses

344   to the 20 light pulses can be seen on the patch located in the superficial and deep colliculus

345   (approximately electrodes 150 to 250, spanning ~1000 um in depth). We aligned the

346   histological slices including the probe tract with the Allen Brain Atlas, which allowed us to

347   overlay the probe location with the fUSi data of the same coronal slice (Figure 6E). The spiking

348   activity is indicated as a color-coded bar on top of the fUSi data. We averaged and normalized

349   the fUSi data pooled from 6 brains along the Neuropixels probe track and compared it to the

350   spiking activity. In this recording, we found a correlation coefficient between the fUSi and

351   spiking signal of 0.83 (Figure 6E Right). We generally found a stronger correlation between

352   the spiking activity and the fUSi signal in fUSi experiments with stronger responses (Figure 6F;

353   correlation coefficient r = 0.69; n = 26 probe recordings).

354   **Optogenetic response patterns are different in the colliculus and downstream targets**

355   Next, we asked how the optogenetic activation of neurons in the SC propagates through its

356   direct and indirect output circuit elements. To this end we analyzed optogenetic responses in

357   6 different brain areas (Figure S5): 1) the superficial SC (sSC), 2) the deep SC (dSC), 3) The

358   periaqueductal gray (PAG) which has previously been linked to aversive behaviors [50–52], 4) the

359   pulvinar (LP), which is a direct target of NTSR neurons, 5) The caudal caudoputamen (CPc),

360   and 6) the posterior paralaminar nuclei of the thalamus (PPnT), which have not previously

361   been linked to innate aversive behaviors but were strongly activated during NTSR stimulation

362   (Figure 5H).

363   In all six areas, we found that the population of single neurons responded well to the

364   optogenetic stimulation (Figure 6G first column). Similar to the raw spiking analysis, each area

365   contained single neurons that responded well to all 20 pulses throughout the

366   1 s stimulation (Figure 6G second column) as well as cells that responded to the first

367   stimulation only and others that were inhibited by further pulses (Figure 6G fourth column).

368   We found that both the amplitude and the temporal changes in the spiking activity

369   corresponded well to the fUSi signal recorded in the same brain areas (Figure 6G last column).

370   When accounting for the delayed and slower blood response, the temporal profile of the fUSi

371   signal and the probe recordings were similar for each of the tested areas. Areas with a stronger

372   signal in the fUSi experiments showed a corresponding stronger spiking response (Figure 6G),

373   and areas that showed a decrease in blood flow also showed a decrease in firing rate (Figure

374   S6B and S6C).

375   To quantify the neural responses during the 20 optogenetic pulses, we calculated the mean,

376   background-subtracted response of each responding neuron to the 40 ms after each pulse,

377   normalized these 20 measurements to its maximal response and calculated the area under the

378   curve (AUC) of those 20 values. An AUC of 1 indicates a cell that responds equally well to all

379   20 pulses, whereas negative AUC values indicate more inhibition than excitation. The resulting

380   activity maps sorted by AUC indicate a different distribution of optogenetic responses in the

381   different areas (Figure 6H; sSC n = 101 units, dSC n = 392, PAG n = 225, LP n = 199, CPc

382   n = 517, PPnT n = 196). We found a higher proportion of sustained responses (high AUC) in

383   the superficial SC, more transient responses in the PPnT, CPc and periaqueductal gray, and

384   a higher percentage of inhibited neurons in the pulvinar (Figure 6I). Subsequently, we then

385   clustered the optogenetic responses into 6 types (Figure 6J). Neurons from the superficial SC

386   were mostly in the more sustained clusters 1-3. Late-onset neurons (cluster 4) were almost

387   absent in the SC but found in the other four multi-synaptic targets. Transient responses (cluster

388   5) are the dominant response type in the PPnT and inhibition was found in the pulvinar and

389   PPnT (cluster 6). Taken together, these results show that optogenetic stimulation could be

390   traced from the SC across several synapses. Response patterns were different at different

391   stages downstream of NTSR neurons and the temporal profile of area-specific activity

392   measured using spike recordings or fUSi corresponded well with each other.

Visual responses downstream of NTSR neurons

394   Activation of pulvinar-projecting neurons has been shown to induce arrest behavior [7,17] and we

395   found arrest-like behavior when activating NTSR neurons (Figure 1). In addition, NTSR

396   neurons respond well to visual stimuli mimicking attacking and over-head flying predators [38]

397   that induce aversive behaviors [19,20]. We thus tested whether neurons at different stages in the

398   NTSR output circuitry that respond to optogenetic activation of NTSR neurons would also

399   respond to behaviorally relevant visual stimuli. We found responses to a looming stimulus

400   mimicking an attacking predator in optogenetically activated neurons in all tested brain areas

401   (Figure 7A; sSC: 31 out of 57 optogenetically activated neurons, dSC: 76/139, PAG: 58/60, LP:

402   25/44, CPc: 59/109, PPnT: 14/50). Neurons showed different response properties including

403   early and late onset responses as well as transient and continuous activity, and inhibition to a

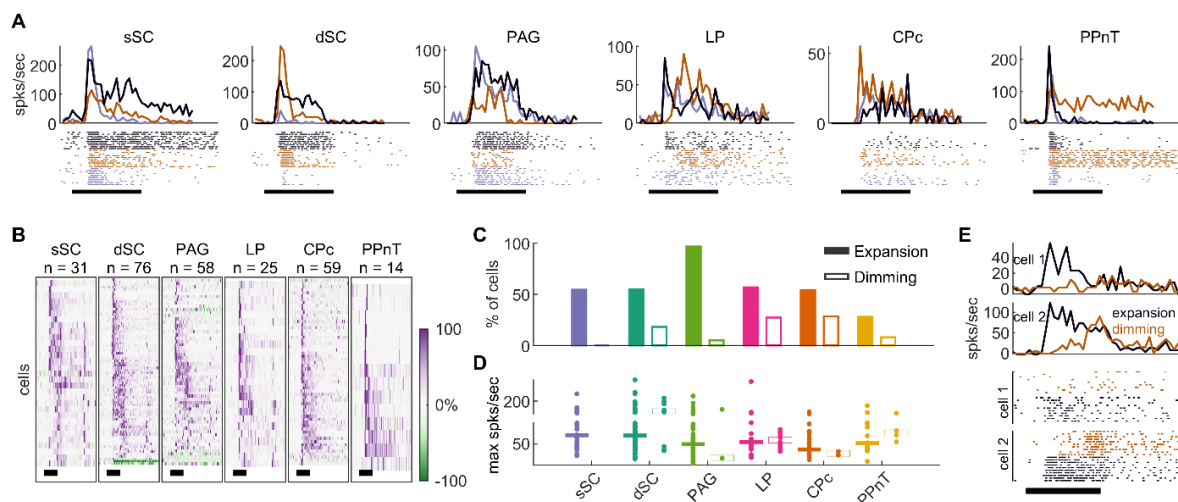404   looming visual stimulus. These activation patterns were distributed differently in the six tested

Figure 7. Visual responses in optogenetically activated cells of the NTSR-circuit. A. Example responses (raster and spikes/s) to a black looming stimulus for 3 cells with median response strength for each area. Black bar indicates time of looming (0.315 s). **B.** Normalized responses to a black looming disk of all optogenetically activated cells with looming responses in each area. **C.** Percentage of optogenetically activated cells with looming or dimming responses. 100% for looming/dimming for sSC n = 57/6, dSC n = 139/44, PAG n = 60/59, LP n = 44/44, CPc n = 109/7, PPnT n = 50/50. **D.** Maximal response strength to expansion and dimming stimuli for each responding cell and their median per area. **E.** Example of cell with looming, but without dimming response (cell 1), and an example cell responding to both (cell 2).

405 brain areas (Figure 7B). It is known that stimuli with similar properties as looming, but without
406 ecological relevance, e.g. a dimming stimulus, do not elicit aversive behaviors [19]. In accordance
407 with these behavioral findings, we could not detect responses to the dimming stimulus in
408 optogenetically activated neurons of the sSC (Figure 7C). Neurons in further downstream
409 areas sometimes responded to dimming stimuli at similar strength as for looming (Figure 7D
410 and 7E). However, in all areas, fewer neurons responded to dimming stimuli as compared to
411 looming stimuli (sSC: 0 out of 6 optogenetically responding cells, dSC: 8/44, PAG: 3/59, LP:
412 12/44, CPc: 2/7, PPnT: 4/50). We found no dimming responses in the sSC even when including
413 units that did not respond to optogenetic stimulation and similar higher percentages of
414 dimming responses in the LP, CPc, and PPnT (Figure S6). These data show that ecologically
415 relevant visual information is present throughout the multi-synaptic downstream networks of
416 the colliculus that is revealed during opto-fUSi imaging.

417 **Inhibition of PPnT facilitates habituation to repeated stimulation of NTSR neurons.**
418 The PPnT has not been previously shown to participate in collicular driven behaviors. Our fUSi
419 data showed that it is consistently activated in response to the stimulation of CAMKII, NTSR
420 and PV neurons of the colliculus (Figure 5). We corroborated that neurons in the PPnT respond
421 to both optogenetic stimulation of NTSR neurons and visual stimuli (Figure 6 and 7). To
422 investigate its role in defensive behaviors, we chemogenetically suppressed activity of its
423 neurons while optogenetically stimulating NTSR neurons in the SC. We injected an AAV coding
424 for the inhibitory DREADDs hM4D(qi) under human synuclein 1 promoter into the PPnT of
425 NTSRxChR2 mice (Figure 8A-B). The same optogenetic stimulation protocol as in previous
426 experiments was used to activate ChR2 in NTSR neurons. We tested mice in the open field
427 arena (Figure 1A) and optogenetically stimulated (20 Hz for 1 s) as the mouse crossed the
428 center of the arena. We conducted five experimental sessions, separated by at least 2 days
429 (Figure 8A). To inhibit the PPnT, clozapine N-oxide (CNO) was injected intra-peritoneally 20-
430 30 minutes before the beginning of the second session.

431 We found that inhibition of PPnT increased the variability in the responsiveness of mice to the
432 optical stimulation (Figure 8C-E). This variability manifested as a decrease in the probability
433 that arrest would be triggered by the optogenetic stimulus after a CNO injection (Figure 8F,
434 Movie S17 and Movie S18). During subsequent sessions mice did not regain the lost
435 behavioral response (Figure 8G) and tended to maintain a higher speed than controls during
436 the stimulation periods (Figure 8H).

437 To investigate the relationship between stopping behavior and the specific location of hM4D
438 expression in the PPnT, we examined the correlation between stopping probability in Session
439 2 (when CNO was first administered) and the coordinates of the center of expression (Figure
440 S7A-C), or the antero-posterior spread of the expression (Figure S7D). Linear regression
441 revealed weak correlations with the AP, ML, DV planes and extent of expression (Pearson
442 coefficient r=0.112, 0.245, -0.293 and -0.297 respectively). Additionally, we compared the
443 stopping probability of animals with and without DREADD expression in the different areas
444 included in the PPnT (Figure S7E). All the examined mice had expression in the POL. The PoT
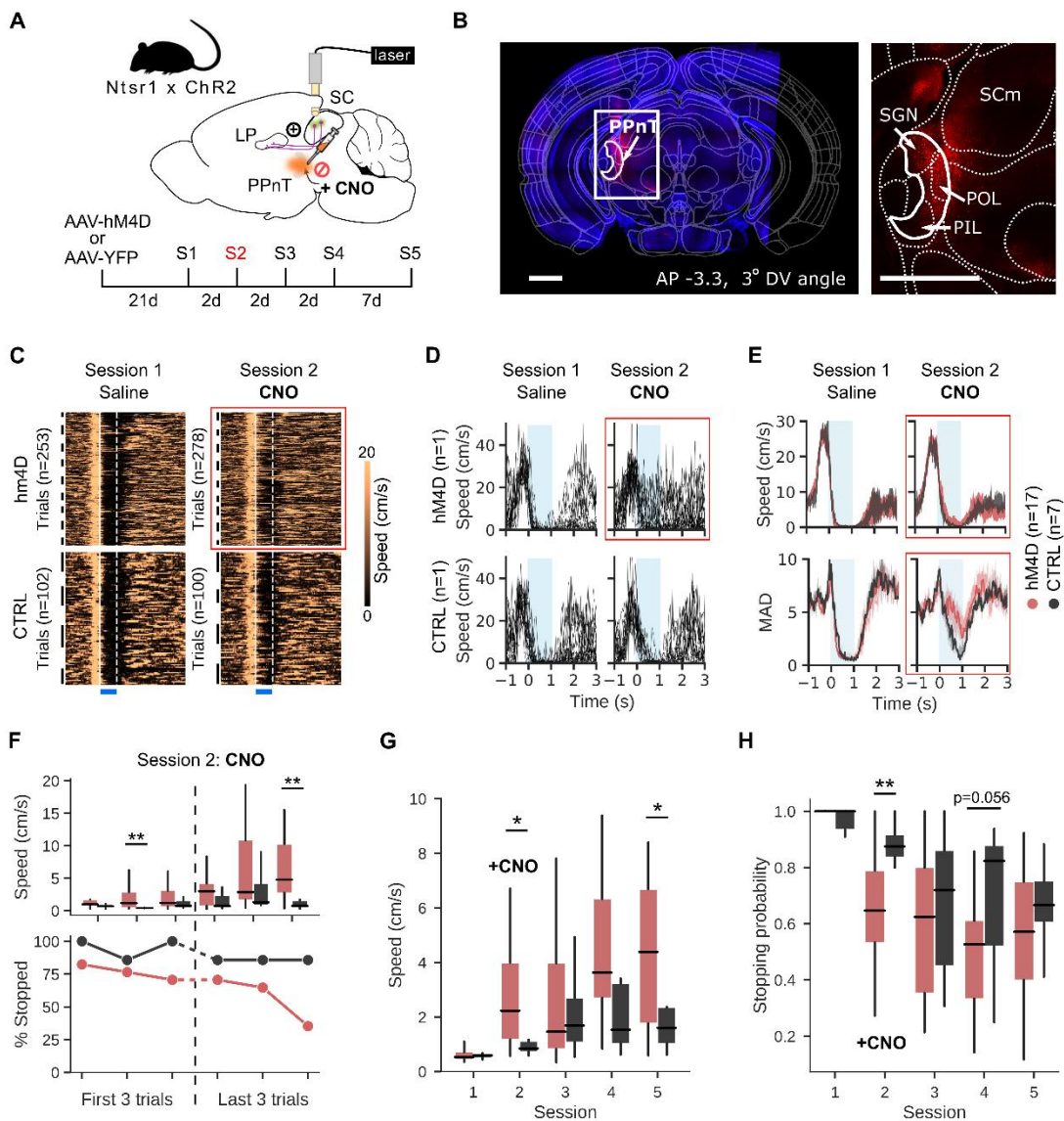445 was present in most animals (n=13/17), but the presence or absence of expression in this area

446

Figure 8. PPnT inhibition facilitates habituation to repeated optogenetic stimulation. A. Experimental paradigm **B.** Expression of AAV2-hSyn-hM4D(Gi)-mCherry (red) in the PPnT of a NTSR x Chr2 mouse. Left, coronal brain section aligned to Allen Mouse brain atlas. White rectangle indicates injection site and corresponds to right, zoomed in area. Scale bar 1 mm. **C.** Speed traces of NTSR x Chr2 mice injected with AAV-hM4D (Top row, n=17) and controls (n=7, Bottom row), injected with AAV-YFP for session 1 (saline) and session 2 (CNO). Black lines delineate trials belonging to single animals. White lines delineate onset and offset of optogenetic stimulus. **D.** Speed traces from all trials in session 1 (Left) and 2 (Right) from one example animal from each group. **E.** Top row: median speed traces from all hM4D (red) and CTRL (gray) mice during sessions 1 and 2. Bottom row: mean absolute deviation of the speed for hM4D (red) and CTRL (gray) mice. **F.** Median speed (Top row) and stopping probability (Bottom row) during the one second stimulation of hM4D (red) and CTRL (gray) mice, within the session where CNO was administered. **G.** Median speed of hM4D (red) and CTRL (gray) mice, during the 1 s stimulations across sessions **H.** Stopping probability of hM4D (red) and CTRL (gray) mice, during the 1 s stimulations across sessions. Box plots indicate median, interquartile range, and 5th to 95th percentiles of the distribution. *p < 0.05; **p < 0.01.

20

447 did not change the effect on stopping probability (Mann-Whitney U-test; p=0.198).
448 Interestingly, expression in the PIL and SGN was observed in approximately 50% of the
449 animals (PIL: n=9/17; SGN: n=8/17) and rather than causing the behavioral attenuation,
450 expression in these areas seemed to interfere with the effect, increasing stopping probability
451 (Mann-Whitney U-test; PIL: p=0.037; SGN: p=0.042). We also observed viral expression in the
452 most caudal part of the LP in several animals (n=8/17), but its presence did not correlate with
453 a reduced stopping probability (Mann-Whitney U-test; p=0.168, Figure S8F). Overall, these
454 results suggest that the inhibition of the PPnT, most likely through the POL, facilitates
455 habituation to the repeated activation of collicular NTSR neurons.

456 **Discussion**
457 In this study, we combined fUSi with optogenetics to reveal the whole-brain neuronal networks
458 that link individual cell-types of the SC with a triggered behavior. We show here that the mouse
459 colliculus distributes information encoded in specific cell-types through distinct networks that
460 share a set of common nodes. Three principals have emerged from this work. First, the spatial
461 and temporal activity patterns evoked by each cell-type are distinct from each other. Second,
462 the observed differences (or similarities) in behavior could not be explained by the activity in
463 any single brain region but appear to be the consequence of distributed activity across many,
464 predominately, subcortical brain areas. Third, while fUSi imaging revealed activation of known
465 downstream targets of each cell-type, it also revealed activity in a set of areas previously not
466 considered as part of these behavioral networks. This allowed us to uncover a putative role of
467 one of these novel targets, the PPnT, in habituation. Direct measurements of neural activity
468 using silicon probes demonstrate a strong correspondence in both space and time between
469 the fUSi signal and mean firing rate in each brain region. Using probe recordings, we also
470 found responses to ecologically relevant visual stimuli in brain regions identified as part of the
471 functional network. Taken together, these results support the notion that in the SC individual
472 cell-types trigger distinct behaviors, not via single dedicated pathways, but instead via distinct
473 brain-wide networks that share a common set of nodes.

474 **Collicular cell-types activate different, partially overlapping downstream networks.**
475 A variety of previous lines of evidence are consistent with our finding that activation of different
476 cell-types of the SC and their output pathways leads to the broad yet restricted propagation of
477 information across the brain. We found that each collicular cell-type relayed information
478 through a different downstream network, that converge in a few key nodes (Figure 4 and 5).
479 Our fUSi experiments show that activation of each cell-type modulated the neural activity of at
480 least 68 and up to 193 brain areas. Among the pathways activated were a set of areas that are
481 consistent with known output pathways of the SC and that have been identified to trigger
482 freezing and escape behaviors [6,7,10,12–14,50]. Here we demonstrate that activation of the same
483 neural populations results in neural activity in a much larger than expected set of downstream
484 areas. This extensive dissemination of information is likely due in part to recurrent connectivity
485 within the SC [12,16], as well as recurrent feedback loops with, for example, deeper layers of the
486 SC, PAG, thalamus and PBG [14]. While we do observe the previously reported activity in specific

487 nuclei, brain-wide fUSi allowed us to observe functional networks downstream of cell-types in
488 the SC across the most of the brain.

489 Conversely, the brain-wide activity we observed shows a higher degree of specificity than we
490 would predict from meso-scale maps of area-to-area connectivity [53]. If, for example, we assume
491 each brain area, like the retinal recipient layers of the SC, projects to at least 6 downstream
492 structures we only need 3 synapses to modulate 216 brain areas. In many cases this
493 underestimates the number of projections a brain area makes. The retina sends projections to
494 approximately 40 targets [54], while the primary visual cortex innervates at least 18 cortical and
495 subcortical areas [55]. We saw our maximal spread of activity when stimulating CAMKII neurons,
496 which modulated 246 areas during the early phase, while NTSR neurons modulated 146 areas.
497 This restriction in the extent of dissemination is likely due to the cell-type specific connection
498 made in the SC and other brain regions. In the SC, distinct output pathways are known to
499 selectively sample retinal inputs and project to selected downstream areas [13,56]. In addition,
500 outputs of the SC to the LP have been shown to be relayed to a narrow set of downstream
501 targets in the visual cortex and amygdala [17,48]. This cell-type and pathway specific relay of
502 information is a common feature of several brain structures investigated, including the visual
503 cortex, amygdala and VTA [55,57,58].

504 **Optogenetically triggered behavior can be explained by network activity**
505 How the SC routes the cell-type specific information to evoke different behaviors
506 corresponded well with the observed similarities and differences in the network activity. We
507 observed that activation of CAMKII and NTSR neurons each resulted in an interruption of
508 locomotor activity, which was reflected in the similarity in the brain-wide activity evoked by
509 each cell population (Figure 4). While activating CAMKII and NTSR neurons each interrupted
510 locomotor activity, activating CAMKII neurons resulted in prolonged periods of immobility as
511 compared to NTSR neurons (Figure 1), which corresponded well with the observed
512 differences in the temporal response profiles (Figure 5). For example, in comparison to NTSR,
513 stimulation of CAMKII neurons evoked prolonged activity in areas including the premammillary
514 nucleus of the hypothalamus (PMH) and the superior central nucleus raphe (CS). In addition,
515 we demonstrated that activation of PV and GAD2 neurons facilitated active avoidance and
516 orienting movements, respectively. In comparison to CAMKII and NTSR, activation of PV and
517 GAD2 neurons was characterized by increases in the activity of cerebellar areas like CENT2
518 and IP. To further discuss how different behaviors are mediated, we focus below on three brain
519 areas: the subthalamic nucleus (STN), the cuneiform nucleus (CUN) and midline thalamus
520 nuclei.

521 First, activating either CAMKII or NTSR neurons resulted in increase in the activity of the
522 subthalamic nucleus (STN) – a region involved in the interruption of ongoing behaviors [59,60]. In
523 contrast, the activity of STN was suppressed or not detectable after stimulation of PV and
524 GAD2 cell-types, where locomotion was not interrupted. This suggests that the STN is either
525 activated to pause ongoing behaviors or silenced to promote escape strategies. Second, we
526 found distinct temporal responses in the CUN across mouse lines. The CUN has been shown
527 to trigger freezing and escape [44], participate in the initiation and control of locomotion [61,62] and

528   modulate cardiovascular response [63]. We observed fast, transient responses in animals with
529   freezing-like behaviors (CAMKII, NTSR) and slow, more sustained responses, in animals with
530   continuous locomotion (PV, GAD2). It is therefore plausible that different neuronal
531   subpopulations of the CUN are functionally connected with different collicular cell-types to play
532   various roles in defensive behaviors. Third, we demonstrated that the nuclei of ventral midline
533   thalamus (RE and Xi), which play a role in decision making when exposed to threat [64], are
534   modulated by both PV and CAMKII neurons but in opposite direction, with sustained activation
535   and inhibition, respectively (Figure 5). Taken together our results suggest that opto-fUSi is a
536   reliable method for studying how the cell-type specific information is disseminated from the
537   SC across the brain to trigger behavior.

Opto-fUSi reveals new players in aversive behavior driven by the SC

539   In our experiments, we observed areas consistently activated that have not previously been
540   reported to be involved in mediating visually guided aversive behaviors. Precise circuit
541   dissections have highlighted three major pathways that pass information about visual threat
542   from the SC to downstream areas. These cell-type specific pathways include projections to
543   the amygdala through the LP or the PBG [6,7,17]; and projections to the dPAG [50]. These
544   dissections have led to an atomistic understanding of how the SC mediates aversive behaviors.
545   Here we observed activity in many areas across the brain and four of them captured our
546   attention, namely: the caudal part of caudoputamen (CPc), postrhinal visual area (VISpor),
547   posterior lateral part of the midbrain reticular formation (MRNpl) and PPnT (Figure 5). Some
548   of these areas have been implicated in modulation of visual behavior [65–68]. The PPnT stood out
549   during visual inspection of activity maps of the brain, as it was both reliably activated upon
550   optogenetic stimulation of NTSR neurons of the SC and during the presentation of visual
551   stimuli. The PPnT is known for its role in associative learning during auditory fear conditioning
552   and in mediating fear discrimination and extinction [69,70]. Our experiments revealed that this
553   group of areas play a similar role in behaviors triggered by the SC by acting to suppress
554   habituation. Our results are consistent with the proposed role of PPnT in fear extinction and
555   suggest that PPnT is part of the pathway downstream of the SC and is involved in mediating
556   behaviors triggered from the SC. These results highlight the power of combining optogenetic
557   manipulations with brain-wide observation of neuronal activity, which provides a method to
558   identify the brain-wide networks involved and thus the design experiments that allow us to
559   build a more complete picture of how defensive behaviors are controlled.

Optogenetics and the relationship between fUSi and neural activity

561   One of the key questions for fUSi imaging is the degree to which it faithfully represents the
562   underlying neural activity. In the context of fMRI, while it is generally accepted that the
563   measured blood oxygen-level dependent (BOLD) signal changes are associated with neuronal
564   activity [71]; how and where the BOLD signal reliably represents the spiking activity of individual
565   neurons still remains an open question [72]. Like fMRI, fUSi also relies on the indirect
566   measurement of neural activity through hemodynamic changes, in this case, in cerebral blood
567   volume. Recently, it has been shown that fUS signals, can reliably represent both increases
568   and decreases in local neuronal activity [28,33]. We provide additional evidence that the changes

23

569   in blood volume detected by the fUSi are consistent with the local changes in neuronal activity
570   in a number of different brain regions including parts of the cortex, striatum, hippocampus,
571   thalamus and midbrain (Figure 6 and Figure S6).

572   Light delivery into the brain, similar to our optogenetic activation, has been reported to cause
573   local temperature changes and arterial vasodilation in naïve mice and rats that can cause
574   artefactual signals both in opto-fMRI and opto-fUSi [73,74]. To minimize such potential effects, in
575   our experiments, we used shorter and lower light intensity stimuli (0.3-0.4 mW, 2ms pulses,
576   20-50 Hz, 1 s) than the energy threshold calculated (<1 mW, 20 ms pulses, 20 Hz, 2 s) by
577   Rungta et al. 2017. We did not observe any hemodynamic signal in control experiments using
578   naïve mice in these conditions, indicating that the results reported in this study are driven by
579   the activation of collicular cell-types. In addition, we found that the magnitude, sign, and time
580   course of the fUSi signal corresponded well with the local spiking activity measured in the
581   same area of the brain and in response to the same stimuli.

582   **Brain-wide mapping of function using Opto-fUSi**
583   Understanding the neural basis of defensive behaviors is relevant not only because these
584   behaviors are important for survival, but also because their dysregulation may contribute to
585   anxiety and post-traumatic disorders. To accomplish this, it is necessary to have a holistic
586   understanding of how the nervous system integrates information to guide appropriate
587   behaviors, as well as to know how molecularly defined components of the nervous system
588   contribute to this neuronal activity. Here, we have presented a set of experiments that highlight
589   how combining optogenetics with fUSi can bridge this divide, enabling both the manipulation
590   of targeted components of the nervous system and the simultaneous monitoring of brain-wide
591   activity.

592   Various methods enable us to look at activity across large parts of the brain, including fMRI,
593   wide-field calcium imaging, large-scale electrophysiology, and genetic markers of neural
594   activity. However, fMRI suffers from low temporal and spatial resolution [75,76]. Cortical wide
595   calcium imaging and large-scale probe recordings have excellent temporal and spatial
596   resolution but only allow for measurements that are limited to cortex, in the case of calcium
597   imaging, or in thin columns near the electrode tract for silicon probe recordings [3,77,78]. Finally,
598   genetic markers that putatively report elevated levels of neural activity (e.g. cfos or CaMPARI)
599   provide single cell resolution across the whole brain but have poor temporal resolution and
600   their activation is difficult to interpret [79,80].

601   fUSi enables access to the whole brain at a spatial and temporal resolution (~100 μm^3, 0.1 s)
602   that allowed us to map the neural network activated by defined cell populations of the SC
603   across a larger portion of the brain. To our knowledge, this is the first time a comprehensive
604   brain-wide mapping has been done at this spatiotemporal resolution of the circuits involved in
605   innate defensive behaviors of mice. Previous experiments in humans and primates have
606   provided evidence of the involvement of structures such as the LC, the PAG, the SC, the visual
607   thalamus, the amygdala, the insular cortex and PFC [23–25,81–83]. In rodents, molecular (cfos)
608   functional brain maps have implicated a few additional thalamic, hypothalamic and cerebellar

24

609   areas in various fearful conditions [64,84–88]. We analyzed the activity of 264 areas across the

610   mouse brain. Our results indicate that the neural pathways involved in mediating and

611   modulating the behavioral responses to activation of the SC stimuli is far more complex that

612   previously reported. We believe combining fUSi with targeted cell-type manipulations and

613   natural stimuli will allow us to understand how different brain regions act in concert to guide

614   defensive behaviors under a variety of conditions.

615

ACKNOWLEDGMENTS

AUTHOR CONTRIBUTIONS

Arnau Sans Dublanc, Conceptualization, Data curation, Formal analysis, Funding acquisition, Validation, Investigation, Visualization, Methodology, Writing—original draft, Writing—review and editing; Anna Chrzanowska, Conceptualization, Data curation, Funding acquisition, Investigation, Visualization, Methodology, Writing—original draft, Writing—review and editing; Katja Reinhard, Conceptualization, Data curation, Supervision, Funding acquisition, Investigation, Visualization, Methodology, Writing—original draft, Writing—review and editing; Dani Lemmon, Data curation, Funding acquisition, Investigation, Visualization; Gabriel Montaldo, Conceptualization, Methodology, Software, Supervision, Writing—review and editing; Alan Urban, Conceptualization, Funding acquisition, Methodology, Software, Supervision, Writing—review and editing; Karl Farrow, Conceptualization, Software, Formal analysis, Supervision, Funding acquisition, Investigation, Visualization, Methodology, Writing—original draft, Project administration, Writing—review and editing.

References

1. Zeng, H. & Sanes, J. R. Neuronal cell-type classification: challenges, opportunities and the path forward. *Nat. Rev. Neurosci.* **18**, 530–546 (2017).

2. Stringer, C. *et al.* Spontaneous behaviors drive multidimensional, brainwide activity. *Science (80-.).* **364**, (2019).

3. Steinmetz, N. A., Zatka-Haas, P., Carandini, M. & Harris, K. D. Distributed coding of choice, action and engagement across the mouse brain. *Nature* **576**, 266–273 (2019).

4. Ahrens, M. B. *et al.* Brain-wide neuronal dynamics during motor adaptation in zebrafish. *Nature* **485**, 471–477 (2012).

5. Aimon, S. *et al.* Fast near-whole–brain imaging in adult Drosophila during responses to stimuli and behavior. *PLOS Biol.* **17**, e2006732 (2019).

6. Shang, C. *et al.* A parvalbumin-positive excitatory visual pathway to trigger fear responses in mice. *Science (80-.).* **348**, 1472–1477 (2015).

7. Shang, C. *et al.* Divergent midbrain circuits orchestrate escape and freezing responses to looming stimuli in mice. *Nat. Commun.* **9**, 1232 (2018).

8. Hoy, J. L., Bishop, H. I. & Niell, C. M. Defined Cell Types in Superior Colliculus Make Distinct Contributions to Prey Capture Behavior in the Mouse. *Curr. Biol.* **29**, 4130-4138.e5 (2019).

9. Masullo, L. *et al.* Genetically Defined Functional Modules for Spatial Orienting in the Mouse Superior Colliculus. *Curr. Biol.* **29**, 2892-2904.e8 (2019).

10. Zhang, Z. *et al.* Superior Colliculus GABAergic Neurons Are Essential for Acute Dark Induction of Wakefulness in Mice. *Curr. Biol.* **29**, 637-644.e3 (2019).

11. Ellis, E. M., Gauvain, G., Sivyer, B. & Murphy, G. J. Shared and distinct retinal input to the mouse superior colliculus and dorsal lateral geniculate nucleus. *J. Neurophysiol.* **116**, 602–610 (2016).

12. Gale, S. D. & Murphy, G. J. Distinct cell types in the superficial superior colliculus project to the dorsal lateral geniculate and lateral posterior thalamic nuclei. *J. Neurophysiol.* **120**, 1286–1292 (2018).

13. Gale, S. D. & Murphy, G. J. Distinct representation and distribution of visual information by specific cell types in mouse superficial superior colliculus. *J. Neurosci.* **34**, 13458–13471 (2014).

14. May, P. J. The mammalian superior colliculus: Laminar structure and connections. *Progress in Brain Research* **151**, 321–378 (2006).

15. Inayat, S. *et al.* Neurons in the Most Superficial Lamina of the Mouse Superior Colliculus Are Highly Selective for Stimulus Direction. *J. Neurosci.* **35**, 7992–8003 (2015).

16. Whyland, K. L., Slusarczyk, A. S. & Bickford, M. E. GABAergic cell types in the superficial layers of the mouse superior colliculus. *J. Comp. Neurol.* **528**, 308–320 (2020).

17. Wei, P. *et al.* Processing of visually evoked innate fear by a non-canonical thalamic pathway. *Nat. Commun.* **6**, 6756 (2015).

18. Zhang, Z. *et al.* Superior Colliculus GABAergic Neurons Are Essential for Acute Dark Induction of Wakefulness in Mice. *Curr. Biol.* **29**, 637-644.e3 (2019).

677   19.   Yilmaz, M. & Meister, M. Rapid innate defensive responses of mice to looming visual
678   stimuli. *Curr. Biol.* **23**, 2011–2015 (2013).

679   20.   De Franceschi, G., Vivattanasarn, T., Saleem, A. B. & Solomon, S. G. Vision Guides
680   Selection of Freeze or Flight Defense Strategies in Mice. *Curr. Biol.* **26**, 2150–2154
681   (2016).

682   21.   Lee, H. J. *et al.* Activation of Direct and Indirect Pathway Medium Spiny Neurons Drives
683   Distinct Brain-wide Responses. *Neuron* **91**, 412–424 (2016).

684   22.   Nakamura, Y. *et al.* fMRI detects bilateral brain network activation following unilateral
685   chemogenetic activation of direct striatal projection neurons. *Neuroimage* **220**, 117079
686   (2020).

687   23.   Almeida, I., Soares, S. C. & Castelo-Branco, M. The distinct role of the amygdala,
688   superior colliculus and pulvinar in processing of central and peripheral snakes. *PLoS*
689   *One* **10**, (2015).

690   24.   Liddell, B. J. *et al.* A direct brainstem-amygdala-cortical 'alarm' system for subliminal
691   signals of fear. *Neuroimage* **24**, 235–243 (2005).

692   25.   Terpou, B. A. *et al.* The Innate Alarm System and Subliminal Threat Presentation in
693   Posttraumatic Stress Disorder: Neuroimaging of the Midbrain and Cerebellum. *Chronic*
694   *Stress* **3**, 247054701882149 (2019).

695   26.   Bernal-Casas, D., Lee, H. J., Weitz, A. J. & Lee, J. H. Studying Brain Circuit Function
696   with Dynamic Causal Modeling for Optogenetic fMRI. *Neuron* **93**, 522-532.e5 (2017).

697   27.   Mace, E. *et al.* Functional ultrasound imaging of the brain: theory and basic principles.
698   *IEEE Trans. Ultrason. Ferroelectr. Freq. Control* **60**, 492–506 (2013).

699   28.   Macé, É. *et al.* Whole-Brain Functional Ultrasound Imaging Reveals Brain Modules for
700   Visuomotor Integration. *Neuron* **100**, 1241-1251.e7 (2018).

701   29.   Urban, A. *et al.* Chronic assessment of cerebral hemodynamics during rat forepaw
702   electrical stimulation using functional ultrasound imaging. *Neuroimage* **101**, 138–149
703   (2014).

704   30.   Rabut, C. *et al.* 4D functional ultrasound imaging of whole-brain activity in rodents. *Nat.*
705   *Methods* **16**, 994–997 (2019).

706   31.   Brunner, C. *et al.* A platform for brain-wide functional ultrasound imaging and analysis
707   of circuit dynamics in behaving mice. *bioRxiv* (2020). doi:10.1101/2020.04.10.035436

708   32.   Macé, E. *et al.* Functional ultrasound imaging of the brain. *Nat Methods* **8**, 662–664
709   (2011).

710   33.   Aydin, A.-K. *et al.* Transfer functions linking neural calcium to single voxel functional
711   ultrasound signal. *Nat. Commun.* **11**, 2954 (2020).

712   34.   Taniguchi, H. *et al.* A resource of Cre driver lines for genetic targeting of GABAergic
713   neurons in cerebral cortex. *Neuron* **71**, 995–1013 (2011).

714   35.   Madisen, L. *et al.* A toolbox of Cre-dependent optogenetic transgenic mice for light-
715   induced activation and silencing. *Nat. Neurosci.* **15**, 793–802 (2012).

716   36.   Gerfen, C. R., Paletzki, R. & Heintz, N. GENSAT BAC cre-recombinase driver lines to
717   study the functional organization of cerebral cortical and basal ganglia circuits. *Neuron*
718   **80**, 1368–1383 (2013).

719 37. Madisen, L. *et al.* A robust and high-throughput Cre reporting and characterization
720   system for the whole mouse brain. *Nat. Neurosci.* **13**, 133–140 (2010).

721 38. Gale, S. D. & Murphy, G. J. Active Dendritic Properties and Local Inhibitory Input Enable
722   Selectivity for Object Motion in Mouse Superior Colliculus Neurons. *J. Neurosci.* **36**,
723   9111–23 (2016).

724 39. Rubin, J. M. *et al.* Fractional moving blood volume: estimation with power Doppler US.
725   *Radiology* **197**, 183–190 (1995).

726 40. Rubin, J. M., Bude, R. O., Carson, P. L., Bree, R. L. & Adler, R. S. Power Doppler US: a
727   potentially useful alternative to mean frequency-based color Doppler US. *Radiology*
728   **190**, 853–856 (1994).

729 41. Lein, E. S. *et al.* Genome-wide atlas of gene expression in the adult mouse brain. *Nature*
730   **445**, 168–176 (2007).

731 42. Sparks, D. L. The brainstem control of saccadic eye movements. *Nat. Rev. Neurosci.* **3**,
732   952–964 (2002).

733 43. Isa, T. & Sasaki, S. Brainstem control of head movements during orienting; Organization
734   of the premotor circuits. *Prog. Neurobiol.* **66**, 205–241 (2002).

735 44. Dean, P., Redgrave, P. & Westby, G. W. M. Event or emergency? Two response systems
736   in the mammalian superior colliculus. *Trends Neurosci.* **12**, 137–147 (1989).

737 45. Herkenham, M. New Perspectives on the Organization and Evolution of Nonspecific
738   Thalamocortical   Projections.   in   403–445   (Springer,   Boston,   MA,   1986).
739   doi:10.1007/978-1-4613-2149-1_11

740 46. Harting, J. K., Updyke, B. V. & Van Lieshout, D. P. Striatal projections from the cat visual
741   thalamus. *Eur. J. Neurosci.* **14**, 893–896 (2001).

742 47. Takahashi, T. The organization of the lateral thalamus of the hooded rat. *J. Comp.
743   Neurol.* **231**, 281–309 (1985).

744 48. Beltramo, R. & Scanziani, M. A collicular visual cortex: Neocortical space for an ancient
745   midbrain visual structure. *Science (80-.).* **363**, 64–69 (2019).

746 49. Bennett, C. *et al.* Higher-Order Thalamic Circuits Channel Parallel Streams of Visual
747   Information in Mice. *Neuron* **102**, 477-492.e5 (2019).

748 50. Evans, D. A. *et al.* A synaptic threshold mechanism for computing escape decisions.
749   *Nature* **558**, 590–594 (2018).

750 51. Watson, T. C., Cerminara, N. L., Lumb, B. M. & Apps, R. Neural correlates of fear in the
751   periaqueductal gray. *J. Neurosci.* **36**, 12707–12719 (2016).

752 52. Deng, H., Xiao, X. & Wang, Z. Periaqueductal gray neuronal activities underlie different
753   aspects of defensive behaviors. *J. Neurosci.* **36**, 7580–7588 (2016).

754 53. Oh, S. W. *et al.* A mesoscale connectome of the mouse brain. *Nature* **508**, 207–214
755   (2014).

756 54. Martersteck, E. M. *et al.* Diverse Central Projection Patterns of Retinal Ganglion Cells.
757   *Cell Rep.* **18**, 2058–2072 (2017).

758 55. Han, Y. *et al.* The logic of single-cell projections from visual cortex. *Nature* **556**, 51–56
759   (2018).

760   56.   Reinhard, K. *et al.* A projection specific logic to sampling visual inputs in mouse superior
761   colliculus. *Elife* **8**, (2019).

762   57.   Beier, K. T. *et al.* Topological Organization of Ventral Tegmental Area Connectivity
763   Revealed by Viral-Genetic Dissection of Input-Output Relations. *Cell Rep.* **26**, 159-
764   167.e6 (2019).

765   58.   Fadok, J. P. *et al.* A competitive inhibitory circuit for selection of active and passive fear
766   responses. *Nature* **542**, 96–99 (2017).

767   59.   Aron, A. R. & Poldrack, R. A. Cortical and subcortical contributions to stop signal
768   response inhibition: Role of the subthalamic nucleus. *J. Neurosci.* **26**, 2424–2433
769   (2006).

770   60.   Fife, K. H. *et al.* Causal role for the subthalamic nucleus in interrupting behavior. *Elife* **6**,
771   1–13 (2017).

772   61.   Capelli, P., Pivetta, C., Esposito, M. S. & Arber, S. Locomotor speed control circuits in
773   the caudal brainstem. *Nature* **551**, 373–377 (2017).

774   62.   Mori, S., Sakamoto, T., Ohta, Y., Takakusaki, K. & Matsuyama, K. Site-specific postural
775   and locomotor changes evoked in awake, freely moving intact cats by stimulating the
776   brainstem. *Brain Res.* **505**, 66–74 (1989).

777   63.   Korte, S. M., Jaarsma, D., Luiten, P. G. M. & Bohus, B. Mesencephalic cuneiform nucleus
778   and its ascending and descending projections serve stress-related cardiovascular
779   responses in the rat. *J. Auton. Nerv. Syst.* **41**, 157–176 (1992).

780   64.   Salay, L. D., Ishiko, N. & Huberman, A. D. A midline thalamic circuit determines reactions
781   to visual threat. *Nature* **557**, 183–189 (2018).

782   65.   Reig, R. & Silberberg, G. Article Multisensory Integration in the Mouse Striatum. *Neuron*
783   **83**, 1200–1212 (2014).

784   66.   Nagy, A., Eördegh, G., Norita, M. & Benedek, G. Visual receptive field properties of
785   neurons in the caudate nucleus. *Eur. J. Neurosci.* **18**, 449–452 (2003).

786   67.   Schulz, J. M. *et al.* Short-latency activation of striatal spiny neurons via subcortical visual
787   pathways. *J. Neurosci.* **29**, 6336–6347 (2009).

788   68.   Wilson, J. S., Hull, C. D. & Buchwald, N. A. Intracellular studies of the convergence of
789   sensory input on caudate neurons of cat. *Brain Res.* **270**, 197–208 (1983).

790   69.   Grosso, A., Santoni, G., Manassero, E., Renna, A. & Sacchetti, B. A neuronal basis for
791   fear discrimination in the lateral amygdala. *Nat. Commun.* **9**, (2018).

792   70.   Gross, C. T. & Canteras, N. S. The many paths to fear. *Nature Reviews Neuroscience*
793   **13**, 651–658 (2012).

794   71.   Logothetis, N. K. & Wandell, B. A. Interpreting the BOLD signal. *Annu. Rev. Physiol.* **66**,
795   735–769 (2004).

796   72.   Ekstrom, A. How and when the fMRI BOLD signal relates to underlying neural activity:
797   The danger in dissociation. *Brain Res. Rev.* **62**, 233–244 (2010).

798   73.   Rungta, R. L., Osmanski, B. F., Boido, D., Tanter, M. & Charpak, S. Light controls
799   cerebral blood flow in naive animals. *Nat. Commun.* **8**, (2017).

800   74.   Christie, I. N. *et al.* FMRI response to blue light delivery in the naïve brain: Implications

801   for combined optogenetic fMRI studies. *Neuroimage* **66**, 634–641 (2013).

802   75.   Jung, W. B., Shim, H. J. & Kim, S. G. Mouse BOLD fMRI at ultrahigh field detects
803   somatosensory networks including thalamic nuclei. *Neuroimage* **195**, 203–214 (2019).

804   76.   Lewis, L. D., Setsompop, K., Rosen, B. R. & Polimeni, J. R. Fast fMRI can detect
805   Oscillatory neural activity in humans. *Proc. Natl. Acad. Sci. U. S. A.* **113**, E6679–E6685
806   (2016).

807   77.   Allen, W. E. *et al.* Global Representations of Goal-Directed Behavior in Distinct Cell
808   Types of Mouse Neocortex. *Neuron* **94**, 891-907.e6 (2017).

809   78.   Omlor, W. *et al.* Context-dependent limb movement encoding in neuronal populations
810   of motor cortex. *Nat. Commun.* **10**, (2019).

811   79.   Moeyaert, B. *et al.* Improved methods for marking active neuron populations. *Nat.*
812   *Commun.* **9**, 1–12 (2018).

813   80.   Morgan, J. I. & Curran, T. Stimulus-transcription coupling in the nervous system:
814   Involvement of the inducible proto-oncogenes fos and jun. *Annual Review of*
815   *Neuroscience* **14**, 421–451 (1991).

816   81.   Koizumi, A. *et al.* Threat anticipation in pulvinar and in superficial layers of primary visual
817   cortex (V1). Evidence from Layer-Specific Ultra-High Field 7T fMRI. *eNeuro* **6**, (2019).

818   82.   Shiba, Y. *et al.* Converging Prefronto-Insula-Amygdala Pathways in Negative Emotion
819   Regulation in Marmoset Monkeys. *Biol. Psychiatry* **82**, 895–903 (2017).

820   83.   Morris, J. S., DeBonis, M. & Dolan, R. J. Human amygdala responses to fearful eyes.
821   *Neuroimage* **17**, 214–222 (2002).

822   84.   Chou, X. L. *et al.* Inhibitory gain modulation of defense behaviors by zona incerta. *Nat.*
823   *Commun.* **9**, (2018).

824   85.   Mendes-Gomes, J. *et al.* Defensive behaviors and brain regional activation changes in
825   rats confronting a snake. *Behav. Brain Res.* **381**, (2020).

826   86.   Cho, J. H., Rendall, S. D. & Gray, J. M. Brain-wide maps of Fos expression during fear
827   learning and recall. *Learn. Mem.* **24**, 169–181 (2017).

828   87.   Vianna, D. M. L., Borelli, K. G., Ferreira-Netto, C., Macedo, C. E. & Brandão, M. L. Fos-
829   like immunoreactive neurons following electrical stimulation of the dorsal
830   periaqueductal gray at freezing and escape thresholds. *Brain Res. Bull.* **62**, 179–189
831   (2003).

832   88.   Mongeau, R., Miller, G. A., Chiang, E. & Anderson, D. J. Neural correlates of competing
833   fear behaviors evoked by an innately aversive stimulus. *J. Neurosci.* **23**, 3855–3868
834   (2003).

835   89.   Babcock, D. S., Patriquin, H., LaFortune, M. & Dauzat, M. Power Doppler sonography:
836   basic principles and clinical applications in children. *Pediatr. Radiol.* **26**, 109–115
837   (1996).

838   90.   Jun, J. J. *et al.* Fully integrated silicon probes for high-density recording of neural
839   activity. *Nature* **551**, 232–236 (2017).

840   91.   Brainard, D. H. The Psychophysics Toolbox. *Spat. Vis.* **10**, 433–436 (1997).

841   92.   Pelli, D. G. The VideoToolbox software for visual psychophysics: Transforming numbers

842   into movies. *Spat. Vis.* **10**, 437–442 (1997).

843   93.   Mathis, A. *et al.* DeepLabCut: markerless pose estimation of user-defined body parts
844   with deep learning. *Nat. Neurosci.* **21**, 1281–1289 (2018).

845   94.   Lopes, G. *et al.* Bonsai: an event-based framework for processing and controlling data
846   streams . *Frontiers in Neuroinformatics* **9**, 7 (2015).

847   95.   Friston, K. J. *et al.* Analysis of fMRI time-series revisited. *Neuroimage* **2**, 45–53 (1995).

848   96.   Benjamini, Y. & Hochberg, Y. Controlling the False Discovery Rate: A Practical and
849   Powerful Approach to Multiple Testing. *J. R. Stat. Soc. Ser. B* **57**, 289–300 (1995).

850   97.   Szekely, G. J. & Rizzo, M. L. Hierarchical clustering via joint between-within distances:
851   Extending Ward's minimum variance method. *J. Classif.* **22**, 151–183 (2005).

852   98.   Rousseeuw, P. J. Silhouettes: A graphical aid to the interpretation and validation of
853   cluster analysis. *J. Comput. Appl. Math.* **20**, 53–65 (1987).

854   99.   Davies, D. L. & Bouldin, D. W. A Cluster Separation Measure. *IEEE Trans. Pattern Anal.*
855   *Mach. Intell.* **PAMI**-**1**, 224–227 (1979).

856   100.   Shamash, P., Carandini, M., Harris, K. & Steinmetz, N. A tool for analyzing electrode
857   tracks from slice histology. *bioRxiv* 447995 (2018). doi:10.1101/447995

858   101.   Yger, P. *et al.* A spike sorting toolbox for up to thousands of electrodes validated with
859   ground truth recordings in vitro and in vivo. *Elife* **7**, (2018).

860   102.   Segev, R., Goodhouse, J., Puchalla, J. & Berry, M. J. Recording spikes from a large
861   fraction of the ganglion cells in a retinal patch. *Nat. Neurosci.* **7**, 1154–1161 (2004).

862   103.   Baden, T. *et al.* The functional diversity of retinal ganglion cells in the mouse. *Nature*
863   **529**, 345–50 (2016).

864   104.   Calinksi, T. & Harabasz, J. A dendritic method for cluster analysis. *Comm. Stat.* **3**, 1–27
865   (1974).

866

Methods

Animals

All experimental procedures were approved by the Ethical Committee for Animal Experimentation (ECD) of the KU Leuven and followed the European Communities Guidelines on the Care and Use of Laboratory Animals (004–2014/EEC, 240–2013/EEC, 252–2015/EEC). Male and female adult (2-4 months old) transgenic mice were used in our experiments including, *Ntsr1-GN209Cre, Ai9, Thy1-STOP-YFP, Ai32 x Ntsr1-GN209Cre, Ai32 x PvalbCre and Ai32 x Gad2Cre. Ntsr1-GN209Cre* mice (Genset: 030780-UCD) express Cre recombinase in *Ntsr1-GN209* expressing neurons. *Ai9* (JAX: 007909) and *Thy1-STOP-YFP* (JAX: 005630) are reporter lines that express tdTomato and YFP fluorescent proteins respectively, when in presence of the Cre recombinase. *Ai32* (JAX: 012569) is a reporter line that expresses Channelrhodopsin2 in presence of Cre recombinase. *PvalbCre* mice express Cre recombinase in parvalbumin-expressing neurons. *Gad2Cre* mice express Cre recombinase in *Gad2*-expressing neurons. Mice were kept on a 12:12 h light:dark cycle and sterilized food pellets and water were provided *ad libitum.* Experiments were performed during the light phase.

General surgical procedures

Anesthesia was induced at the beginning with an intraperitoneal injection of Ketamine (100 mg/kg) and Medetomidine (1 mg/Kg). Before starting any surgical procedure, the paw of the animal was pinched to check for the absence of pedal reflex. After deep anesthesia was achieved, mice were placed in a stereotaxic workstation (Narishige, SR-5N), on a homeothermic blanket to keep a stable body temperature. Eye ointment was applied to protect the eyes from drying and from light (Dura tear, NOVARTIS, 288/28062–7) and Lidocaine (0.5%, 0.007 mg/g body weight) was injected under the skin above the skull. The surgical areas were shaved and the skin was disinfected using iso-betadine. Then, the skin was cut following the midline and retracted to the sides to expose the skull. Anterior-posterior coordinates are measured from Bregma.

Viral injections

Once the skull was exposed, a hole was performed at the right coordinates by gently rotating a needle against the skull. We used micropipettes (Wiretrol II capillary micropipettes, Drumond Scientific, 5-000-2005) with an open tip of around 30 μm, prepared with a Laser-Based Micropipette Puller (Sutter Instrument, P-2000), and an oil-based hydraulic micromanipulator MO-10 (Narishige) for all stereotactic injections. To trace back the injection sites, we coated the glass pipette tip with DiD (Thermo, D7757).

For optogenetic experiments, we targeted *CamkII*-expressing neurons of the retinorecipient layers of the colliculus by injecting wild type mice with AAV2-CamkII-hChR2(E123T/T159C)-p2A-EYFP-WPRE (UNC vector core, AV5456B). We used *Ai9* and *Thy1-STOP-YFP* mice as wild type mice. We injected 200–300 nl of AAV in 100 nl doses with a waiting time of 5–10 min after each injection. Coordinates for the superficial colliculus were AP: -3.6 to 3.8, ML: -0.2 to -0.3, DV: -1.1 to -1.4. To express ChR2 specifically in *Ntsr1-GN209* expressing neurons of the

33

907 colliculus, we injected 200–300 nl of AAV2-EF1a-DIO-hChR2(E123T/T159C)-p2A-EYFP-
908 WPRE (UNC vector core, AV5468C) into the superficial colliculus of *Ntsr1-GN209Cre* mice.

909 For chemogenetic experiments, we injected 300 nl of AAV2-hSyn-hM4D(Gi)-mCherry
910 (Addgene, 50475), or AAV2-hSyn-EYFP (UNC vector core, AV4376E) as control, into the
911 PPnT. PPnT coordinates: AP -3 to -3.4, ML -1.8 to 2, DV: -3.5 to -3.3.

912 Following injection, the skin was glued with Vetbond tissue adhesive (3M,1469) to close the
913 wound. Next, mice were injected with painkillers (Buprenorphine 0.2 mg/kg I.P.) and antibiotics
914 (Cefazolin 15 mg/kg I.P.) and were allowed to recover on top of a heating pad. After recovery
915 from anesthesia, animals were provided with soft food and water containing antibiotics
916 (emdotrim, ecuphar, BE-V23552) and were monitored for 3 days and administrated
917 Buprenorphine and Cefazolin depending on the condition of the animal. Any following surgery
918 was performed 21 days after injection to allow for proper gene expression.

919 **Cranial Windows and optic-fiber cannula Implantations**

920 *opto-fUSi*
921 Once the mouse was anesthetized and the skull was exposed, the lateral and posterior
922 muscles were retracted. Vetbond was applied to open skin and exposed muscle, and a
923 titanium head plate was attached to the skull using dental cement (Superbond C&B, Prestige-
924 dental). Then a cranial window extending over almost the whole extent of the left hemisphere
925 and part of the right hemisphere (AP: +2 to -6.5mm, ML 1.5 to -4.5) was made with a drill.
926 Then, an optic-fiber cannula (Doric Lenses, MF1.25, 200/245-0.37, FLT) was implanted. The
927 entry point of the fiber into the brain was AP: -3.6 to -3.8, ML +1.5 at a 56° angle. The fiber was
928 slowly inserted 1.8 mm into the brain so that the tip would be placed at ML: 0 and DV: -1.1 to
929 -1.2. Next, a ring of dental cement was formed around the craniotomy and the optic-fiber to
930 stabilize the whole preparation. Finally, the cranial window was covered with silicone elastomer
931 for protection and the mouse was allowed to recover on a heating pad. Mice were treated with
932 painkillers (Buprenorphine 0.2 mg/kg I.P.), antibiotics (Cefazolin 15 mg/kg I.P.) and anti-
933 inflammatory (Dexamethasone 0.1 mg/kg) drugs for 5 days.

934 *In vivo electrophysiology*
935 Once the mouse was anesthetized and the skull was exposed, Vetbond was applied to open
936 skin and exposed muscle, and a titanium head plate was attached to the skull using dental
937 cement (Superbond C&B, Prestige-dental). Then, cranial windows (~0.5 to 1 mm^2) were
938 performed over the coordinates of the target regions. The following coordinates were used as
939 the center of craniotomies: SC: AP: -3.7, ML: -0.5; PPnT: AP: -3.3, ML: -1.9; lateral posterior
940 nucleus of the thalamus: AP: -2.1, ML: -1.8; tail of caudate putamen: AP: -1.4, ML: -3.1. An
941 additional hole was made for the implantation of an optic-fiber cannula. The entry point of the
942 fiber into the brain was AP: -3.6 to -3.8, ML: +1.5 at a 56° angle. The fiber was slowly inserted
943 1.8 mm into the brain so that the tip would be placed at ML: 0 and DV: -1.1 to -1.2.

944 **Opto-open field test**
945 All behavioral experiments were performed in a custom made square wooden box (W: 50 cm
946 x L: 50 cm x H: 36 cm). Dim ambient light (~50 lux) was provided by a lamp (Paulmann Licht

947 GmbH, PDG09/14) positioned above the arena and oriented away from it, towards a wall.
948 Behavior was recorded at 30 fps using a camera (Point Grey Research, FMVU-03MTM-CS)
949 positioned 53 cm above the center of the arena. For optogenetic activation we used a 473 nm
950 DPSS laser system (Laserglow Technologies, R471003GX) connected to a patchcord with a
951 rotatory joint (Thorlabs, RJPFL2). Optogenetic stimulation was controlled with custom software
952 written in MATLAB. Before every experiment, the output of the laser was measured at 20 Hz
953 or 50 Hz (2 ms pulse width) and set at 0.3-0.4 mW ($9.5 – 12.5$ mW/mm^2). For any given mouse
954 line, a high-frequency stimulus was chosen based on preliminary behavioral data. In those
955 mouse lines where 20 Hz stimulation did not evoke any visible response, the following
956 experiments were done at 50 Hz. In the data shown here, CAMKII and NTSR mice were
957 stimulated at 20 Hz whereas PV and GAD2 were stimulated at 50 Hz.

958 5 days after implantation of the optic fiber, mice were habituated to the handler, patchcord and
959 experimental room for at least 3 days. The day of the test, mice were placed in the center of
960 the arena and were allowed to freely explore for 2 min. After the acclimatization time, when
961 the mice moved away (~10 cm) from the perimeter of the box, towards the center, light
962 stimulation was manually triggered. At any given test, mice where stimulated at high (20 Hz or
963 50 Hz, 20 or 50 pulses) and low (5 Hz, 20 pulses) frequencies in a pseudo-random manner.
964 Time between stimuli was set to be of at least 30 seconds. A typical experiment lasted 20-40
965 min.

966 In tests that combined optogenetics with DREADDs, the experiments where performed as
967 explained above, except that mice were injected with either CNO (2 mg/kg) or saline 30 min
968 prior to the test and where only stimulated at 20Hz.

969 Repeated tests where always separated by at least 48h.

Protocol of Functional Ultrasound Imaging
971 5 days after surgery, mice where habituated to the handler, experimental room and to head-
972 fixation on a platform for 7 days. Then, the awake mouse was head-fixed on the platform and
973 the body movement was partially restrained by a foam shelter. The silicone cap was removed
974 and the cranial window was covered with a 2-3 % agarose layer to reduce brain movement. A
975 473 nm DPSS laser system was then connected to the optic fiber cannula using a ferrule patch
976 cable (Thorlabs, M83L01). Before every experiment, the output of the laser was measured at
977 20 Hz or 50 Hz and set at 0.3-0.4 mW ($9.5 – 12.5$ mW/mm2). Next, acoustic gel (~1 mL, Unigel,
978 Asept) was applied on the agarose for ultrasound coupling and the ultrasound probe (L22-14v,
979 Verasonics) was lowered down to a distance of ~3 mm from the brain. The probe was moved
980 along the lateral axis by a linear microprecision motor (Zaber, X-LRM-DE). At the beginning of
981 each session, a reference anatomical scan was acquired for registration (53 sagittal planes
982 from lateral +1.5 mm to -5 mm, 125 μm steps). Following, we acquired the functional scan (23
983 sagittal planes, from lateral +1.5 mm to -4.5 mm, 250 μm steps). Two optogenetic stimuli were
984 applied at each plane (high and low frequencies) before moving to the next one. For each
985 stimulus, functional images were acquired for 20 s (10 Hz), and the stimulus was applied after
986 a 10 s baseline. The functional imaging and optogenetic stimulation were controlled and

987   synchronized using custom software written in MATLAB. Optogenetic stimuli consisted of a
988   high (20 Hz, 20 pulses, 2 ms pulse width or 50 Hz, 50 pulses, 2 ms pulse width) and a low (5
989   Hz, 20 pulses, 2 ms pulse width, ~2 mW/mm^2) frequency stimulus. The acquisition of the 23
990   sagittal planes was acquired sequentially starting at lateral -4.5, and the whole craniotomy was
991   imaged 7-12 times per session. Total acquisition time was ~3.5 h.

Generation of a Functional Ultrasound Image

993   This procedure was adapted from the sequence for fast, whole-brain functional ultrasound
994   imaging described in Macé et al., 2018. An ultrasound probe containing a linear array of 128
995   ultrasound emitters/receivers, emitted plane waves (15 MHz, 2 cycles) in five different angles
996   (-6°, -3°, 0°, 3°, 6°). The echoes from each plane wave was acquired with the receivers and
997   adjusted with a time-gain compensation to account for the attenuation of ultrasound signals
998   with depth (exponential amplification of 1 dB/mm). This process generated a single emit-
999   receive image ('B-mode image') for each angle and was applied three times for averaging. The
1000   15 individual B-mode images were then combined (~2 ms, 500 Hz), resulting in a higher quality
1001   image ('compound B-mode image').

1002   50 compound B-mode images were acquired every 100 ms (10 Hz) to generate a functional
1003   ultrasound image. Blood cells flowing inside the vessels scatter back and shift the frequency
1004   of the emitted waves (Doppler effect). Such shifts were measured and extracted in real-time,
1005   using singular-value-decomposition-based spatiotemporal filtering, and high-pass temporal
1006   filtering (cut-off frequency: 20 Hz). From the filtered data, we calculated the mean intensity of
1007   the Doppler signal (Power Doppler) in each voxel. Power Doppler integrates all the Doppler
1008   signals in a voxel to obtain an intensity value that is proportional to the amount of blood cells
1009   moving in that voxel at a given time. Unlike Color Doppler, it lacks information about velocity
1010   or direction of the blood flow but reliably reports hemodynamic changes in blood volume [27,40,89].
1011   The intensity value of a voxel at a given time was calculated as: $I(x,y) = A(x,y,t)^2$ where I is
1012   Power Doppler Intensity, x , y are the coordinates of a given voxel in a given plane, A is the
1013   amplitude of the compound B-mode images after filtering, and t was time. The resulting
1014   functional ultrasound image was 143 x 128 voxels in which each voxel had a size of 52.5 µm x
1015   100 µm x 300 µm [28].

Electrophysiological recordings

1017   12 *NTSR1-GN209-Cre x Chr2 (Ai32)* mice of either sex at the age of 2.5-3 months were used
1018   to record optogenetic and light driven responses in the superior colliculus and PAG (7
1019   recordings), pulvinar (9 recordings), caudateputamen (9 recordings) and posterior
1020   paralaminar nuclei of the thalamus (3 recordings) .

1021   Two days after performing cranial windows, animals were habituated to the recording set up
1022   for 3–4 days. The day of the recording, head-posted animals were fixed on a treadmill or
1023   floating ball in front of a screen. Then, a Neuropixels probe phase 3A (Imec, Belgium) [90] coated
1024   with a fluorescent dye (DiD, Thermofisher) was inserted into the brain with the tip reaching
1025   down to 1-1.5 mm below the target area. Once the right depth was reached, it was left to rest
1026   for 20-30 min, before starting the recording. Artificial cerebrospinal fluid (150 mM NaCl, 5 mM

1027 K, 10 mM D-glucose, 2 mM NaH2PO4, 2.5 mM CaCl2, 1 mM MgCl2, 10 mM HEPES adjusted
1028 to pH 7.4 with NaOH) was used to cover the exposed brain and skull.

1029 Neuropixel probes contain 960 recording sites on a single shaft distributed in two rows of 480
1030 electrodes along 9600 µm (16 µm lateral spacing, 20 µm vertical spacing), of which 384 can
1031 be recorded simultaneously. In all our experiments, we recorded from the 384 electrodes
1032 closest to the tip, spanning 3840 µm. Signals were recorded at 30 KHz using the Neuropixels
1033 headstage (Imec), base station (Imec) and a Kintex-7 KC705 FPGA (Xilinx). High-frequencies
1034 (>300 Hz) and low-frequencies (<300 Hz) were acquired separately. To select the recording
1035 electrodes, adjust gain corrections, observe online recordings, and save data, we used
1036 SpikeGLX software. Timings of visual and optogenetic stimulation were recorded
1037 simultaneously using digital ports of the base station.

1038 While recording from any given location, first, the superior colliculus of these mice received
1039 30 repetitions of blue light trains (20 Hz, 20 pulses, 1 ms pulse width, 0.2 mW) spaced by 20
1040 seconds intervals. Then, visual stimuli were presented.

1041 **Visual stimuli**
1042 Visual stimuli were presented on a 32-inch LCD monitor (Samsung S32E590C, 1920x1080
1043 pixel resolution, 60 Hz refresh rate, average luminance of 2.6 cd/m^2) positioned perpendicular
1044 to the mouse head, at 35 cm from the right eye, so that the screen was covering 90˚ of azimuth
1045 and 70˚ of altitude of the right visual field. Visual stimuli were presented on a gray background
1046 (50% luminance), controlled by Octave (GNU Octave) and Psychtoolbox [91,92]. The visual stimuli
1047 consisted of a small black disc that linearly expanded from 2˚ to 50˚ of diameter within 300 ms
1048 at the center of the screen and a disk of 50° diameter dimming from background to black within
1049 300 ms. The stimuli were repeated 10 times.

1050 **Immunohistochemistry**
1051 Animals were perfused and post-fixed overnight using 4% paraformaldehyde (HistoFix,
1052 Roche). Vibratome sections (100-200 µm) were collected in 1x PBS and were incubated in
1053 blocking buffer (1x PBS, 0.3% Triton X-100, 10% Donkey serum) at room temperature for 1
1054 hour. Then slices were incubated with primary antibodies in blocking buffer overnight at 4°C.
1055 The next day, slices were washed 3 times for 10 min each in 1x PBS with 0.3% TritonX-100
1056 and incubated in secondary antibody solution diluted in blocking buffer overnight at 4°C. We
1057 used rabbit anti-GFP (Thermo Fisher, A-11122, 1:500) as a primary antibody to label Chr2-
1058 positive cells and anti-mCherry (Novus, NBP2-25158, 1:500) to label hM4D-postive
1059 cells. Alexa488 donkey anti-rabbit (Thermo Fisher, A21206, 1:500-1000) and Cy3 donkey anti-
1060 chicken (ImmunoJackson, 703-166-155, 1:1000) were used as secondary antibodies. Nuclei
1061 were stained with DAPI (Roche, 10236276001, 1:500) together with the secondary antibody
1062 solution. Sections were then again washed 3 times for 10 min in 1x PBS with 0.3% TritonX-
1063 100 and 1 time in 1x PBS, covered with mounting medium (Dako, C0563) and a glass
1064 coverslip. Confocal microscopy was performed on a Zeiss LSM 710 microscope. Images of
1065 areas with Chr2- and hMD4-expressing cells, the fiber location and the Neuropixels track
1066 labelled with DiD were obtained using a 10x (plan-APOCHROMAT 0.45 NA, Zeiss) objective.

Analysis of behavioral data

Animal tracking was performed using DeeLabCut software [93]. Stimulus onsets and offsets were extracted with custom-made Bonsai workflow [94]. Tracking data were sorted into peri-stimulus trials using custom made Python scripts. Trials where stimulation happened in the periphery of the setup were not included in the analysis, unless explicitly stated. Behavioral parameters were calculated by pooling all trials per mouse and calculating the average, followed by average over mice. Speed was extracted based on positional data of the base of the tail obtained from DeepLabCut. Frames with probability lower than 0.9 were filtered out and linearly interpolated. Position data were smoothed with a median filter of window size = 5. The preferred body angle (Figure 1G) was obtained by first aligning the trajectories to the same initial position and by rotating them to Cartesian X axis by an angel of their body position at the stimulus onset frame. The body position angle is the angle between the line connecting the tail base with the nose and the Cartesian X axis. Next, the preferred angle was calculated between then line of stimulus onset nose position and stimulus offset nose position. Latency to the corner was analyzed as time needed to reach a corner (corner is defined as a square of 10 x 10 cm) after the stimulation onset.

Analysis of fUSi data

Registration

At the beginning of each session, we acquired a reference anatomical map. These anatomical maps were then registered to the Allen Mouse Brain Common Coordinate Framework version 3 (CCFv3) (Allen Brain API; brain-map.org/api/index.html) (Figure 2D). Registration was done semi-automatically based on anatomical landmarks that could be recognized on both the anatomical map and CCFv3 (external outline of the brain, dorsal hippocampus, 3rd and 4th ventricles, cerebellar outline, middle cerebral sinus, colliculus, and corpus callosum). These landmarks were used to readjust the 3D volume of the reference map to the CCFv3 by applying scaling in either of the x, y, z axis and rotations and translations in the coronal, sagittal or axial planes when necessary. Then, we calculated the rotations and translations of the coronal, sagittal and axial planes to create a 3D transformation matrix (from anatomical map to CCFv3).

Segmentation

fUSi from each session were automatically registered to the CCFv3 using the 3D transformation matrices obtained in the previous steps. Assignment of voxels to brain areas was based on the CCFv3 segmentation. For our analysis, we excluded fiber tracts, ventricles, unsegmented parts of main brain structures (CTX, CTXsp, TH, HY, MB, HB, CB), merged layers of brain areas, and excluded or merged neighboring areas with volumes < 300 μm^3. Our final version of the atlas was comprised of 264 brain areas in one hemisphere of the brain (see Table S2).

Response Time Traces

The relative hemodynamic changes ($\Delta I/I$) were calculated for each voxel, where I was the baseline (mean of 10 s before stimulus onset) and ΔI was the subtraction of the baseline to the

1106   signal at each time point. The traces of the individual areas were obtained for every individual

1107   trial by summing all the voxels assigned to each area (Figure 2E).

1108   *Data filtering and normalization.*

1109   In order to analyze the response traces of each segmented area, first, we created a dataset

1110   with the temporal signals, Ti i=1..Ntime, of each region, trial and session of each animal;

1111 $T_{Animal,repetition}$(region,time). In this dataset, all the trials of the different sessions were added.

1112   Therefore, the repetitions were Nsessions*Ntrials. The intensity signal obtained from the

1113   Power doppler, is susceptible to brain tissue motions caused by the awake animal's

1114   movements. However, motion artifacts can typically be distinguished from hemodynamic

1115   changes based on the shape (noise/real; quick spiky/slow curved), and amplitude (noise/real

1116 $\Delta I/I$; >100%/1-15%) of the signal. In this study, in order to remove trials affected by motion

1117   artifacts we computed the mean temporal signal of each region (Tm) and standard deviation

1118   (SD), and then eliminated outlier values where Ti-Tm were 2.5 times higher than the SD. The

1119   eliminated values were replaced by the previous non-eliminated value. To eliminate the global

1120   variations in the brain (baseline perturbations) we selected the 20% of the regions with lowest

1121   response during a 2 seconds time window after the stimulus onset, then averaged these

1122   regions to create a baseline signal. This baseline signal was then subtracted from all

1123   segmented areas. The resulting normalized temporal traces where used for statistical analysis

1124   (Figure 2G).

1125   *Active Brain Regions*

1126   To determine if a brain region was activated by a stimulus, first, we used the normalized

1127   temporal traces of every trial to calculate a T-score for each animal, using a general linear

1128   model, as commonly used in fMRI [95]. To take into account the different temporal dynamics

1129   present in the responses, the GLM was applied using 1 and 2 seconds stepped (0.5 seconds

1130   steps) time windows, starting at the stimulus onset until 7.5 seconds after stimulus. Next, a

1131   one-sample two-tailed t test was performed on the n T-scores obtained for the n animals. The

1132   region was considered active if the resulting P-value, adjusted for a false discovery rate

1133   (Benjamini and Hochberg FDR procedure), was <0.05 (Figure S4D) [96]. For display (such as in

1134   Figure 2J), we quantified the median response time courses across animals, we standardized

1135   the responses with regard to the values before stimulus onset (z-score) and we corrected for

1136   the relative differences between the stimulation levels of each animal. To do this we calculated

1137   a correction factor from normalizing the peak response (A = average of the signal 0.5s around

1138   the maximal value within a time window after stimulus onset), across all brain areas where:

1139   A_norm(region) = A(region)/sqrt(sum(A(region)^2)), then divided the correction factor across

1140   each time point. The Average of all the corrected response traces, for each mouse line, are

1141   shown in Figure 2J and S2G and are used in the subsequent figures.

1142   *Pixel-to-pixel Activity Maps*

1143   To visualize pixel-to-pixel activity maps, for each voxel, we quantified the median of the

1144   response time courses across trials. We then standardized the responses computing the z-

1145   score, using the 10 seconds before stimulus onset and a 2 seconds time window after stimulus

1146 onset. Next, we averaged activity maps of animals belonging to the same mouse line applied

1147 a median filtering of 4 x 4 pixels on the resulting z-score map. The filtered z-score maps were

1148 used for visual inspection of the brain activity and for data visualization (Figure 5H).

1149 *Clustering of fUSi time courses*

1150 Time course of all active brain regions in the four neuronal groups were clustered using

1151 hierarchical classification and the e-linkage algorithm, an extensions of Ward's minimum

1152 variance method [97]. The optimal number of clusters was determined by visual inspection of the

1153 mean silhouette value [98] and Davies-Bouldin Index [99]. Clustering was only preformed on the

1154 1056 active areas for the 1s optogenetic stimulus.

1155 **Analysis of Neuropixels recordings**

1156 *Raw spiking activity*

1157 To extract spikes from raw Neuropixels data, the average voltage on each electrode in the

1158 0.5 s before onset of the optogenetic stimulation was subtracted from the signal during

1159 stimulation. Spikes were identified using the 'findpeaks' function in MATLAB with a threshold

1160 of 4 standard deviations of the signal before the stimulation. Spikes during the 1 ms of each

1161 light pulse were excluded as they could cause artifacts, especially on the electrodes in the

1162 superior colliculus.

1163 *Activity maps*

1164 Confocal images of brain slices containing the probe tracks were aligned with the Allen Brain

1165 Atlas using the allen CCF tool [100]. This allowed us to identify the same slice of the fUSi data

1166 set. To compare the activity on the probe with the fUSi signal, we averaged the z-scored signal

1167 of x-2 to x+2 pixels for each x location of the probe. The raw spiking data on the whole probe

1168 was resampled to match the resolution of the fUSi data. We normalized each data set

1169 separately to its maximal value, resulting in the plot shown in Figure 6G and analyzed in Figure

1170 6F. Correlation coefficients were calculated using the 'corrcoef' function in MATLAB.

1171 *Spike sorting*

1172 The high-pass filtered in-vivo data was automatically sorted into individual units using SpyKING

1173 CIRCUS [101] with the following parameters: cc_merge = 0.95 (merging if cross-correlation

1174 similarity > 0.95), spike_thresh = 6.5 (threshold for spike detection), cut_off = 500 (cut-off

1175 frequency for the butterworth filter in Hz). Automated clustering was followed by manual

1176 inspection, merging of units if necessary and discarding of noise and multi-units using phy2

1177 (https://github.com/cortex-lab/phy). Units were evaluated based on the average waveform

1178 shape and auto-correlogram. Only cells with < 1% of inter-spike intervals of ≤ 1 ms were

1179 considered and cross correlograms with nearby neurons were inspected to find spikes from

1180 the same neurons [102].

1181 *Detection of responding units*

1182 Peri-stimulus histograms (PSTH) were calculated using a bin size of 20 ms. For detection of

1183 responding cells and for plotting, the mean spikes/s during 0.3 (looming, dimming) or 0.5

1184 seconds (optogenetic stimulus) before stimulus onset were subtracted from the cell's activity.

1185   We calculated a quality index to capture the reliability of a cell's response to the 10-30 stimulus

1186   repetitions. The quality index was defined as $QI = \frac{Var[\bar{C}_r]_t}{Var[C_t]_r}$ with C being the TxR response

1187   matrix, t = time dimension and r = repetition dimension [103]. Cells were labelled as 'responding'

1188   if the maximal z-score during the stimulus exceeded 3 and if the quality index was at least

1189   0.15.

1190   *Transiency measurements*
1191   For response transiency when stimulated with 20 light pulses (optogenetics), the mean

1192   response during the 40 ms after onset of each pulse was normalized to the absolute maximum

1193   of these 20 responses (positive or negative). The transiency of the response was defined as

1194   the area under the curve (AUC), i.e. the sum of these 20 values divided by 20. An AUC of 1

1195   means that the cell responded equally well to all 20 pulses, an AUC of -1 means that the cell's

1196   activity was equally suppressed by each pulse.

1197   *Clustering of optogenetically induced responses*
1198   The normalized responses to the 20 light pulses were clustered using k-means (MATLAB) with

1199   squared Euclidean distance measurement and 1000 replicates. Based on the Calinski-

1200   Harabasz [104] and Davies-Bouldin indices [99], 7 clusters were chosen where one cluster only

1201   contained very few cells with stronger inhibition. These cells were merged with another cluster

1202   consisting of inhibited cells, resulting in 6 total clusters.